Monodisperse Mesoporous Amphiphilic and T-Group Micron Size Silica Particles

Dissertation

der Mathematisch-Naturwissenschaftlichen Fakultät
der Eberhard Karls Universität Tübingen
zur Erlangung des Grades eines
Doktors der Naturwissenschaften
(Dr. rer. nat.)

Vorgelegt von
Akanksha Dohare
aus Gwalior, Indien

Tübingen
2020

Gedruckt mit Genehmigung der Mathematisch-Naturwissenschaftlichen Fakultät der Eberhard Karls Universität Tübingen.

Tag der mündlichen Qualifikation:	17.12.2020
Stellvertretender Dekan:	Prof. Dr. József Fortágh
1. Berichterstatter:	Prof. Dr. Hermann A. Mayer
2. Berichterstatter:	Prof. Dr. Reiner Anwander

This thesis was prepared from January 2017 to June 2020 under the supervision of Prof. Dr.Hermann A. Mayer in the Institute for Inorganic Chemistry at the Eberhard Karls University of Tubingen.

I am very thankful to the Government of India for providing me financial support through the National Overseas Scholarship.

Contributions

Some of the results presented in this thesis have been developed in the collaboration with the Process Technology Analysis, Reutlingen University and Cellular Nanoscience, and NanoBiophysics and Medical Physics, ZMBP, University Tübingen:

Confocal Raman spectroscopy (Chapter 4, Figure 43 and 44) conducted by Ashutosh Mukherjee from Reutlingen University.

In vitro cell line studies (Chapter 4, Figure 47 and 48) and dyeing experiment (Chapter 4, Figure 42) done by Swathi Sudhakar from ZMBP University Tübingen.

Publications

Part of this work has already been published in the following:

Poster:

A. Dohare and H. A. Mayer, Application of Core-Shell Dumbbell Silica Nanoparticles, oral talk for the Conference on Nano-materials, Jiwaji University Gwalior, India, March 09-11, 2018.

A. Dohare, S. Sudhakar, E. Nadler, T. Chassé, Erik Schäffer and H. A. Mayer, Application of Core-Shell Dumbbell Silica Microparticles, poster for the 9th International Colloidal Conference, Sitges, Spain, June 16-19, 2019.

Talk:

A. Dohare and H. A. Mayer, Anisotropic Core-Shell Silica Particles as platform for Drug Delivery, oral talk (virtual) presented in the conference 6th Nano World Congress (NWC) Boston 2020, Boston MA, USA, December 07-09, 2020.

Publication:

A. Dohare, S. Sudhakar, B. Brodbeck, A. Mukherjee, M. Brecht, A. Kandelbauer, E. Schäffer, and Hermann A. Mayer. Simultaneous Delivery of Curcumin and Quercetin with Anisotropic and Amphiphilic Mesoporous Core-Shell Silica Microparticles. (manuscript under preparation).

B. Brodbeck, **A. Dohare**,S. Sudhakar, E. Schäffer, A. Kandelbauer, T. Chassé, Hermann A. Mayer. Control of shape and morphology of anisotropic dense core-shell micron silica particles. (manuscript under preparation).

Acknowledgment

I would like to thank for the kind help and support of the people who are acknowledged here to complete my doctoral thesis.

My heartily gratitude goes to my doctoral supervisor, Prof. Dr. Hermann A. Mayer to accepting me into his research group for the willingness to supervise the topic. His dedicated support, attention, the intensive discussion, and suggestions which he was always ready to do and without his countless scientific discussion, without his constant support it would have not been complete my thesis.

I greatly appreciate all my colleagues Björn Brodbeck, Dr. Dennis Max Meisel, Dr. Fabian During, Fabio Fait, Dr. Farhad Jafarli, Tomasz Misztal, and Stefanie Wagner for their valuable support, numerous discussions and the wonderful time. Thanks for discussions of Max Koch and Biwen Wang and all praktikant and the base of synthesis of dumbbell silica particles started from the work of Dr. Farhad Jafarli. A further collaborative work was carried out from the group of Prof. Dr. Marc Brecht to describe the drug loaded dumbbell particles by Raman spectroscopy.

My sincere thanks also goes to ZMBP, Cellular Nanoscience for the group of Prof. Erik Schäffer and Prof. Tilman E. Schäffer from NanoBiophysics and Medical Physics, University Tübingen for providing space in their research groups to complete my experiments.

The analytical data formed the scientific basis of this work. Therefore I would like to thank all the people who gave me access to the equipments measurements and evaluation, I am grateful to Miss Elke Nadler and Prof. Thomas Chassé for providing me with plentiful SEM and TEM data with lot of smiles and interest throughout my PhD time. Her interest to explain the results for one of my favourite project was appreciated. I also want to thanks to Ms Kristina Strohmaier for performing the solid-state NMR measurements and Mr. Wolfgang Bock for measuring elementary analysis. My special thanks to Miss Sabine Ehrlich helped me out for all kinds of administrative work and was very supportive. I would also thank Miss Natja Wettering for assisting me with IT problems.

I would like to convey thanks to Dr. Leilei Luo and Lorenz Bock and for conducting the BET measurement every time on a very short notice, Ashutosh Mukherjee for the numerous

recordings of the Raman spectra to describe the drug loaded dumbbell particles by Raman spectroscopy, and Dr. Krishan Kumar to assisting me for data plotting.

I want to thanks my family and all friends who were helped me and guided me during my PhD studies.

Last but not the least, my parents without you I would have never achieved anything. I would like to express countless thanks to my sister. My pillar my husband Dr. Sujan Singh Bimal without you I would have not reached here. I can't thank you enough for being with parents when I couldn't. I am deeply grateful for your contribution in our small family. Thank you for being my constant inspiration.

Dedicated to my family

Table of Contents

Abbreviation ..... **I**

Summary ..... **III**

Zusammenfassung ..... **V**

Chapter 1. Introduction **1**

Chapter 2. Theoretical discussion **3**

2.1 Sol-gel process 3

2.2 Stöber process 3

2.3 Microemulsion process 4

2.4 Nomenclature 5

2.5 Core-shell materials 6

2.6 Anisotropic particles 7

2.7 Mesoporous silica materials 8

Chapter 3. Synthesis of T-group particles **9**

3.1 Introduction 9

3.2 Result and discussion 12

3.2.1 Particles V1-V9 made of vinyltrimethoxysilane (VTMS) 12

3.2.1.1 Influence of the reaction time 12

3.2.1.2 Influence of the molar ratio of VTMS and TEOS particles V7-V9 14

3.2.2 Particles P1-P18 made of Phenyltrimethoxysilane (PTMS) 14

3.2.2.1 Influence of hexane P3,P5 and P6 15

3.2.2.2 Influence of toluene particles P7-P10 17

3.2.2.3 Influence of mesitylene particles P11-P13 17

3.2.2.4 Effect on particles by varying the stirring speed and rate of addition of silane drop 19

3.2.3 Particles M1-M19 made of 3-mercaptopropyltrimethoxysilane (MerTMS) 20

3.2.3.1 Time dependent investigation with TEOS 20

3.2.3.2 Changes in the amount of silanes 22

3.2.3.3 Effect of hexane on the growth of particles 23

3.2.3.4 Effect of *n*-tridecane 24

3.2.3.5 Role of n-tridecane on the partide size and porosity 25

3.2.3.6 Control the morphology and porosity by using mechanical stirrer 27

3.2.4 Physisorption 29

3.2.5 Characteristion of particles 30

3.3 Conclusion 35

Chapter 4. Synthesis of core-shell dumbbell silica particles with simultaneously drug delivery 37

4.1 Introduction 37

4.2 Result and discussion 38

4.2.1 Synthesis of CS1, CS2, DCS1, DCS2, DCS3 and DCS4 microparticles 38

4.2.2 Characterisation of the particles 40

4.2.3 Drug loading efficiency 43

4.2.4 In vitro drug release study 48

4.2.5 Cell viability assay 50

4.3 Conclusion 55

Chapter 5. Experimental Part 56

5.1 General protocol of T group particles 56

5.2 General protocol of dumbbell particles 56

5.3 Solvents, reagents and equipment 56

5.4 Analytics 57

5.5 Drug loading of curcumin (Cur) and quercetin (QT) 59

5.6 In vitro drug release study 59

5.7 Cell viability studies 60

5.8 Experimental table 61

Chapter 6. References 65

Abbreviation

BET	Brunauer-Emmett-Teller
BJH	Barrett-Joyner-Halenda
CS	Core-shell
CMC1/2	Critical Micelle Concentration
CTAB	Cetyltrimethylammoniumbromide
DCS	dumbbell core-shell (Particle)
Cur	Curcumine
DRIFT	Diffuse Reflectance Infrared FourierTtransform (Spectroscopy)
HPDEC	High-power decoupling
HPLC	High performance liquid chromatography
IUPAC	International Union of Pure and Applied Chemistry
KBr	Pottasium bromide
MCM	Mobil Composition of Matter
MTT	3-(4,5-dimethylthiazol-2-yl)-2,5-diphenyl tetrazolium bromide
MTMS	Methyltrimethoxysilan
MerTMS	3-Mercaptopropyltrimethoxysilan
mmol	Milimolar
NMR	Nuclear Magnetic Resonance
O/W	Oil in water
PVA	Polyvinyl alcohol
PTMS	Phenyltrimethoxysilane
QT	Quercetin
SEM	Scanning Electron Microscope
TEM	Transmission Electron Microscope
TEOS	Tetraethoxysilane
TMOS	Tetramethoxysilane
VTMS	Vinyltrimethoxysilane
W/O	Water in oil

d_i	i Quantile of particle diameter (d10, d50, d90)
d^{50}	Median of the particle diameter
h	Hours
nM	Nanomolar
nm	Nanometer
µm	Micrometer
µM	Micromolar
ν	Streching vibration (IR)
δ	Bending vibration (IR)
ν_{as}	Antisymmetric stretching vibration (IR)
ν_s	Symmetrical stretching vibration (IR)

Summary

Organosilica particles of a narrow size distribution made from different silanes (VTMS,PTMS and MerTMS), were prepared by means of a one-step synthesis. In a one-step synthesis, vinyl, phenyl and 3-mercapto-functionalized silica particles with the range of 1.2 to 4.7 µm were synthesized by hydrolysis and condensation using the semi-batch process. The particles are always monodisperse apart from phenyl-functionalized silica particles. Reaction parameters by means the amount of silane, additives (hexane, toluene, mesitylene, *n*-tridecane), stirring speed and dosing rate were systematically investigated and discussed with respect to the target variables particle size, particle size distribution, particle morphology and porosity. All variants as well as the additives dosing rate interaction have a high influence on the particle size, shape and morphology. In most of the cases the addition of additives decreases the final particle size but an addition of *n*-tridecane increases the final particle size. Increasing the amount of TEOS gives a bowl like smaller particles in size while silane (VTMS, PTMS) gives bigger particles with wrinkle a surface. In the presence of *n*-tridecane MerTMS form porous particles in the range from 1- 2 µm but without *n*-tridecane non-porous particles are generated up to 4.7 µm in size. The particles were characterized with different analytical methods. Furthermore, for a better understanding of particle growth, the reaction was followed over time.

Porous microspheres are often used for drug delivery. However, systems for simultaneous delivery of multiple drugs are scarce. Here anisotropic and amphiphilic dumbbell core-shell silica particles were prepared by a simple etching process that can load and release two drugs. The dumbbells consisted of large dense lobes and smaller hollow hemispheres both with shells of mesoporous channels as revealed by electron microscopy. The properly adjusted stirring speed and the application of ammonium fluoride as etching agent determined the shape and the surface anisotropy of the particles. In particular the surface of the dense lobe and the small hemisphere differed in their zeta potentials as confirmed by drug loading experiments. Confocal Raman microscopy and spectroscopy showed that the two polyphenols curcumin (Cur) and quercetin (QT) accumulated in different compartments of the amphiphilic particles. The overall drug loading efficiency of Cur plus QT was high for the amphiphilic particles but differed widely between Cur and QT compared to controls of core-shell silica microspheres

and uniformly charged dumbbell microparticles made by using ammonium carbonate as etching agent. For the amphiphilic particles, we found up to 98 % drug loading and 100 % release efficiency after 6 h at pH 5.5. Furthermore, Cur and QT loaded microparticles showed different cancer cell inhibitory activities. The highest activity was detected for the dual drug loaded amphiphilic microparticles (IC_{50} 13.5 nM) in comparison to the controls. In the longterm, amphiphilic microparticles are promising carriers for the simultaneous delivery of multiple drugs.

Zusammenfassung

Organosilica-Partikel mit enger Größenverteilung, hergestellt aus verschiedenen Silanen (VTMS,PTMS und MerTMS), wurden mittels einer einstufigen Synthese hergestellt. In einer einstufigen Synthese wurden Vinyl-, Phenyl- und 3-Mercapto-funktionalisierte Kieselsäurepartikel im Bereich von 1.2 bis 4.7 µm durch Hydrolyse und anschließende Co-Kondensation von VTMS, PTMS, MerTMS und TEOS nach dem Semi-Batch-Verfahren synthetisiert. Die Partikel sind immer monodispers, abgesehen von phenylfunktionalisierten Kieselsäurepartikeln. Reaktionsparameter mittels der Menge an Silan, Additiven (Hexan, Toluene, Mesitylen, n-Tridecane), Rührgeschwindigkeit und Dosierrate wurden systematisch untersucht und im Hinblick auf die Zielgrößen Partikelgröße, Partikelgrößenverteilung, Partikelmorphologie und Porosität diskutiert. Alle Hauptfaktoren sowie die Interaktion der Dosierrate der Additive haben einen signifikanten Einfluss auf die Partikelgröße, -form und -morphologie. In den meisten Fällen verringert die Zugabe von Additiven die Endpartikelgröße, aber eine Zugabe von n-Tridecan erhöht die Endpartikelgröße. Eine Erhöhung der Menge an TEOS ergibt schüsselartige kleinere Partikel, während Siloxan (VTMS, PTMS) größere Partikel mit faltiger Oberfläche ergibt. In Gegenwart von n-Tridecan bilden MerTMS poröse Partikel im Bereich von 1- 2 µm, aber ohne n-Tridecan erzeugen nichtporöse Partikel eine Größe von bis zu 4.7 µm. Die Partikel wurden mit verschiedenen analytischen Methoden charakterisiert. Darüber hinaus wurde zum besseren Verständnis des Partikelwachstums die Reaktion über die Zeit verfolgt.

Poröse Silicapartikel werden häufig für den Transport von Medikamenten verwendet. Systeme für die gleichzeitige Verabreichung mehrerer Medikamente sind jedoch rar. Hier werden anisotrope und amphiphile Hantel-Kern-Schale-Silicapartikel durch einen einfachen Ätzprozess hergestellt, die zwei Medikamente laden und freisetzen können. Die anistropen Partikel bestehen aus einer großen dichten von einer Schale umgebenen Kugel an die eine kleinere hohle Halbkugel gebunden ist. Die Schalen der großen und kleinen Kugel weisen mesoporösen Kanäle auf, wie die Elektronenmikroskopie ergab. Die richtig eingestellte Rührgeschwindigkeit und die Anwendung von Ammoniumfluorid als Ätzmittel bestimmten die Form und die Oberflächenanisotropie der Partikel. Insbesondere die Oberfläche der großen dichten Kugel und die der kleinen Hemisphäre unterschieden sich in ihren Zetapotentialen, was durch Experimente zur Medikamentenbeladung bestätigt wurde. Konfokale Raman-

Mikroskopie und -Spektroskopie zeigten, dass sich die beiden Polyphenole Curcumin (Cur) und Quercetin (QT) in verschiedenen Kompartimenten der amphiphilen Partikel anreicherten. Die Gesamteffizienz der Wirkstoffbeladung von Cur plus QT war für die amphiphilen Partikel hoch, unterschied sich jedoch stark zwischen Cur und QT im Vergleich zu Kontrollen von Kern-Schale-Silicapartikeln und gleichmäßig geladenen anisotropen Silicapartikeln, die unter Verwendung von Ammoniumcarbonat als Ätzmittel hergestellt wurden. Bei den amphiphilen Partikeln fanden wir bis zu 98 % Wirkstoffbeladung und 100 % Freisetzungseffizienz nach 6 h bei pH 5.5. Darüber hinaus zeigten Cur- und QT-geladene Mikropartikel unterschiedliche krebszellhemmende Aktivitäten. Die höchste Aktivität wurde für die mit zwei Medikamenten beladenen amphiphilen Mikropartikel (IC50 13,5 nM) im Vergleich zu den Kontrollen festgestellt. Auf lange Sicht sind amphiphile Mikropartikel vielversprechende Träger für die gleichzeitige Verabreichung mehrerer Medikamente.

Chapter 1. Introduction

Silicon is one of the most frequently occurring elements on the earth's crust[1] with a mass fraction of approx. 26% and usually bound in the form of silicates or silicon dioxide (silica). Silicon dioxide is present in amorphous or crystalline form are the main components of sand and quartz and contribute up to 90% of the mass of the earth's crust. Due to its unique physical and chemical properties, silica has become increasingly important, not only in research but also in industry.[2–4] Silica has a special position in the production of hybrid particles and is often used as an inorganic matrix for coating. This silica coating has several advantages compared to other inorganic materials.

Synthesis of silica particles in the range of nano to micrometre size is now well known in terms of defined particle sizes and small particle size distribution. However the demands for nano and micro particles as an innovation for modern applications are increasing enormously. In addition, new technology and medical applications require silica particles with different types of functionalities and structures.[5] A general method for the synthesis of inorganic/organic materials is the sol-gel process. In the first step, by means of hydrolysis and condensation reactions, a colloidal suspension of particles in the nanoscale (Sol) is formed, which in the second step unites to form a three dimensional network (Gel). Two distinct processes differentiated the synthesis of silica particles with the acid and base catalysed sol-gel process.[6] In recent years, several modification have been identified, such as the use of surfactants, polymers as a template, variation in precursors and reaction conditions.[7] CTAB is the most commonly used surfactant to prepare highly mesoporous silica nano-/microparticles.[8]

Transportation of drugs into cells for medical diagnostics and treatment is of fundamental importance. Many of the present drugs are suffering from stability problems in a biological environment and/or poor water solubility making the drugs less effective.[9] Thus drug delivery strategies based on different materials have been developed.[9–14]

So far, several types of drug vehicles have been reported which include liposomes,[15] peptides,[16] polymers,[17–19] inorganic nano and microparticles[20–25] and organic/inorganic hybrid materials.[26,27]. A drawback of many materials is their low drug loading capabilities. To improve their therapeutic efficacy large amounts of carrier have to be applied. Unfortunately, most of the carriers are accompanied by drawbacks such as poor biocompatibility, the application of

large amounts of surfactants, the requirement for chemical modifications and complex preparation protocols that restrict their access.

Mesoporous silica nano and microparticles provide networks of pores with a large surface area and high pore volume.[28–31] The opportunity to tailor particle size and shape as well as to tune the pore size on the nanometre scale have made these materials attractive for many applications in different fields.[32–34] Moreover, their intrinsic biocompatibility and biodegradability make mesoporous silica particles ideal platforms for drug delivery systems.[23,33,35,36] By trapping the drug in the mesoporous network, mesoporous silica prevents the degradation of the drugs and can act as a solubility enhancer generating higher solution concentrations compared to the corresponding solid form.[22] Thus, this enhancement has led to a dramatic increase in the interest of mesoporous silica-based formulations in the last decade.[9,37]

This work aims the developing silica particles by using different silanes and additives in the sol-gel process. First part of this work is dedicated to the synthesis of functionalized silica particles with vinyl, phenyl and 3-mercaptopropyl silane. The emphasis is on the systematic determination of the influences of selected reaction parameters on the particle size, shape, morphology and porosity of the silica particles.

In the second part of this work deals with the synthesis of core-shell (**CS**) and anisotropic, amphiphilic dumbbell core-shell (**DCS**) silica particles. The aim is to establish a reproducible method. Furthermore, the particles will be comprehensively/systematically characterised.

Chapter 2. Theoretical discussion

2.1 Sol-gel process [38–41]

The sol-gel process is defined as the synthesis of a sol with the following transition to a gel. The sol is a colloidal dispersion of a solid substance that is distributed very finely in a liquid or gaseous medium. The sol particles must be floated in the solution due to the Brownian motion. A gel is defined as a solid body consisting of two phases. The solid phase forms a network which includes the liquid phase. Through the sol-gel process, a colloidal dispersion (sol) is obtained in a solution of chemical precursors via hydrolysis and condensation processes. Silica sols and silicic acid esters are used as typical production precursors. Hydrolysis and condensation of the precursors can be catalysed both acidically and basically and further take place according to the principles of substitution reactions. In this case, the reaction components hydrolysis and condensation were influenced differently. The sol-gel process is relatively fast in an acidic medium, resulting in numerous very small particles. While in an alkaline medium, as contrast spherical particles were formed, due to the slow hydrolysis reaction produces a stable sol of individual particles. The alcohol used in the sol-gel process acts as a co-solvent which is able to dissolve water and silica precursors. The sol-gel process allows the production of many other types of materials such as fibres, thin films, non-porous glasses and ceramics as well as porous and non-porous, nano and microparticles.[42]

2.2 Stöber process

The Stöber process is a special form of the Sol-gel process. In 1968, Stöber et al. developed a process for the controlled synthesis of monodisperse, non-porous and spherical silica partides in a size range from 0.05 µm to 2.0 µm.[43] The process is based on the ammonia-catalyzed hydrolysis of TEOS and consecutive condensation in the presence of ethanol as solvent.[44,45]
For synthesis, the tetra alkoxy silicate (methyl-, ethyl, n-propyl-, n-butyl-) is used as a precursor, which hydrolyses and condenses in the presence of water and ammonia. There are numerous studies in the literature dealing with the effects of reaction conditions on partide size. However, due to the frequently inconsistent concentration ranges of the reactants, these results are not directly comparable. Therefore, the following statements are kept general.

With more precise control, it is possible to reproduce a certain particle diameter by following parameters for controlling the particle size.

With increasing ammonia concentration[43,46,47], water concentration[48] and chain length of the alkyl residue of the alkoxysilane[43] or alcohol[43] and in the presence of conducting salts[49] , larger particles are formed. High temperature leads to smaller particle sizes. [41,50] The reaction conditions set at the beginning have a significant influence on the resulting particle size and distribution as well as its properties.

Later Bogush et al[51] and LaMer et al[52], have proposed different views on the growth process of silica particles.

The mechanism of Bogush and Zukoski is based on a permanent aggregation of silica particles[51] .In the growth model of LaMer et al;[52] the progressive hydrolysis of the precursor results in the successive increase of the hydrolysed monomer concentration until supersaturation occurs. The supersaturation induces the so-called nucleation, in which nuclei are formed from low-molecular silanes. Consequently, the concentration of dissolved monomers decreases and the nucleation phase ends. The successive condensation of hydrolysed TEOS molecules on the silica particles generates particle growth. [52–54] As long as the critical nucleation concentration is not exceeded again, no new nuclei are formed.

Typical synthesis processes are the batch and semi-batch process. In the batch process, all starting materials are completely added to the reaction solution at the beginning of the synthesis. The high accumulation rate leads to smaller particle sizes and a broader particle size distribution.[55] In the semi-batch process, the precursor is temporarily added to the reaction solution by means of a dosing device. The dosing results in larger particles with a narrower particle size distribution compared to the batch process under identical reaction conditions.[55] A sufficiently low dosing rate ensures that the critical supersaturation concentration is not exceeded again. The renewed exceeding of the supersaturation concentration induces a second nucleation phase and leads to bimodal particle size distributions.

2.3 Microemulsion process

An alternative process for the production of the metal oxide nanoparticles by sol-gel process is the water in oil (W/O) or oil in water (O/W) microemulsion process (Figure 1). Normally water and oil are not miscible, due to the high specific interfacial energy, the total interfacial energy is minimized by phase separation. A microemulsion is an isotropic and

thermodynamically stable single-phase system consisting of three components viz water, oil and surfactants (Figure 1). Surfactant molecules reduce the interfacial surface tension between water and oil. Consequently, the water-loaded micelles are formed, which allow a sol-gel process to take place.[56] In a microemulsion condition, except for thermal variations all micelles exhibit the same size. Thus the micelles in microemulsions are ideally suitable as nanoreactors for synthesis with particle size control.

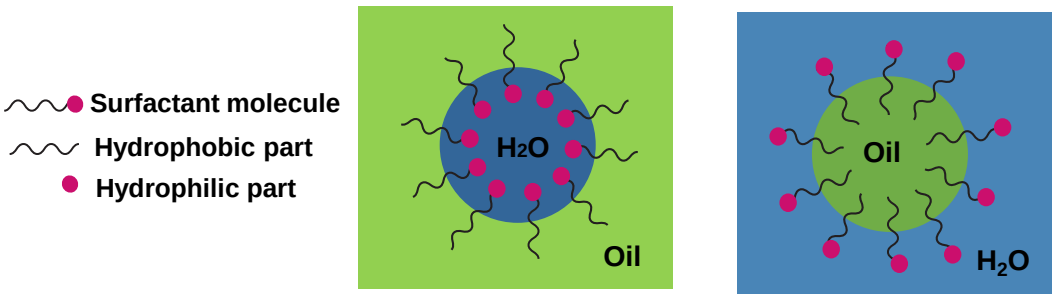

Figure 1: Structure of microemulsion.

One of the main advantages of the microemulsion process is the possibility of encapsulating various nanoparticles in the silica particles. Therefore, this method is used to produce the inorganic core-shell particles. In this process nanoparticles consisting of e.g. silver,[57] cadmium sulphides[58] and iron oxides had already been coated with silica.[59] These coated particles show a good monodispersity and possess a smooth surface.[60] It is interesting to note that, the nanoparticles with hydrophobic ligands can be coated on the surface with silica by microemulsion processes, which has specific significance for the application of these materials in biomedicine.[61]

2.4 Nomenclature

The silane (a brief note about silane) species are classified according to the units attached to a silicon atom into Q, T, D and M groups (Figure 2). The Q groups have four siloxane bonds (Si-O-Si) in a three dimensional structure. In the case of T-groups consisting of three siloxane bonds lead to the formation of two-dimensional layer structures. The D groups only lead to the formation of chains and rings, since only two siloxane bonds can be formed. However the M-groups represent a dimeric form, where only one siloxane bond is formed. With the ^{29}Si solid state NMR spectroscopy the groups can be differentiated. Here the displacement ranges

are characterised between -90 and -110 ppm for Q groups and -50 and -80 ppm for T groups and -10 and -30 ppm for D groups[62].

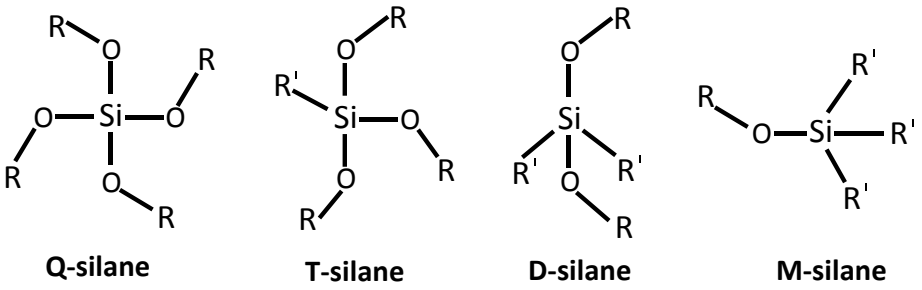

Figure.2 Schematic nomenclature of silica species

2.5 Core-shell silica material

Core-shell particles basically consist of a non-porous shell.[63] These particles are hybrid particles consisting of a core and a shell and there is significant difference in the morphology between the core and shell.[63] The shell part which is made up of a different material or have a different morphology from the core. This allows an extensive combination of different materials and therefore gives access to different types of particles with a wide range of applications.[64] In dependence of the final application the shell materials for the core-shell particles are selected. As illustrated below, the core-shell particles can be classified as follows.[63]

Organic-organic

Organic-inorganic

Inorganic-inorganic

Inorganic-organic

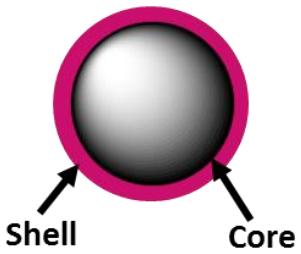

Silica has a specific role in the preparation of core-shell nanoparticles and is also used as a coating matrix since it has various advantages over other inorganic materials.[65] The manipulation of the silica surface makes it possible to synthesize core-with multi shell particles,[66] which has a special significance in the development of multifunctional particles.

2.6 Anisotropic material

In general, monodisperse, spherical particles are used for diagnostics, chromatography or medicine.[67–69] Additional isotropic properties[70] are introduced by subsequent modifications of the particles and the application range is improved. However, production of the particles with complex structure is becoming increasingly important. In the context, it is important to implement anisotropic properties and create multiple morphologies. Anisotropic compounds have diverse features, such as chemical properties, polarity and ability to transform into a single molecule, charge and function in many spatially focused areas.[71]

The term anisotropic particles refers to sol, a substance that can be represented in various forms by targeted synthesis. In comparison to the classical isotropic particles, anisotropic particles have complex shapes. Due to their architecture, anisotropic particles can be classified into four main categories as shown in Figure 3.[72]

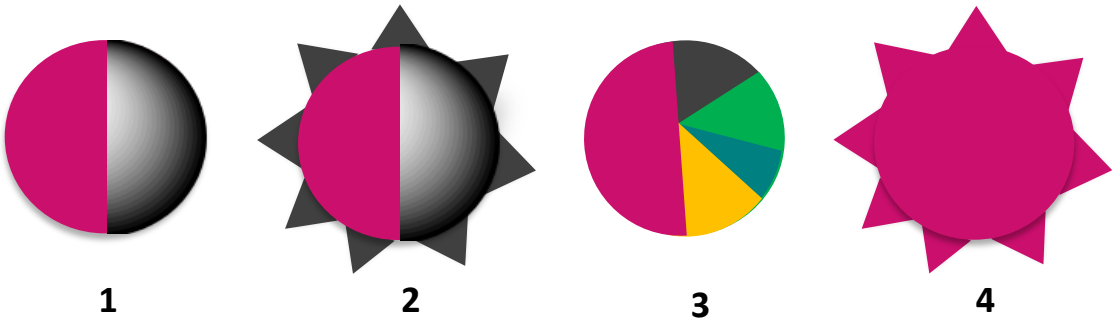

Figure 3: Schemes of anisotropic particles architecture (1) Janus particles; (2) Patchy Janus particles; (3) Multi-compartment particles; (4) Patchy particles

Janus particles have two separate domains. The combination of the different classifications results in patchy Janus particles or patchy multi-compartment particles.[72] The integration of anisotropic properties is achieved by a chemically different structure or surface modification of materials. Janus particles are usually produced by templating, electrospinning or Pickering emulsions.[20–23] Potential applications include stabilisers in emulsions, water-repellent fabrics, catalysis, optical sensors and various devices which are used in medicine.[20, 23]

2.7 Mesoporous silica materials

Porosity can be classified by pore size according to IUPAC, porous materials are divided into micro, meso and macroporous materials on the basis of their pore diameter.[74] The microporous, mesoporous and macroporous materials have pore diameters smaller than 2 nm and between 2 and 50 nm and larger than 50 nm, respectively. The mesoporous silica based materials are an intensely researched class of materials that can be produced by sol-gel processes in the presence of surfactant micelles as templates. The mesoporous ordered silica materials were first published by Mobile Oil Corporation scientists in 1992.[75] The silica materials have characteristic properties, such as highly ordered pore systems with sharp pore size distributions, large specific surfaces and high thermal stability up to 600°C.[76] Most well-known mesoporous silica materials are MCM-41 and MCM-48.[77] The Hexagonal Mesoporous Silica (HMS or wormlike),[78]and materials with large pores diameter are SBA-1,[79] SBA-15[80] and SBA-16.[77,30] The MCM materials belong to a class of the best known mesoporous silica materials. The MCM-48 is composed of two three-dimensional pore networks that are completely independent of each other. Figure 4a, the MCM-48's pore walls consist of X-ray amorphous silica units. Figure 4b, in contrast the MCM-41 has a standard structural arrangement of cylindrical mesopores, which are aligned hexagonally to each other.

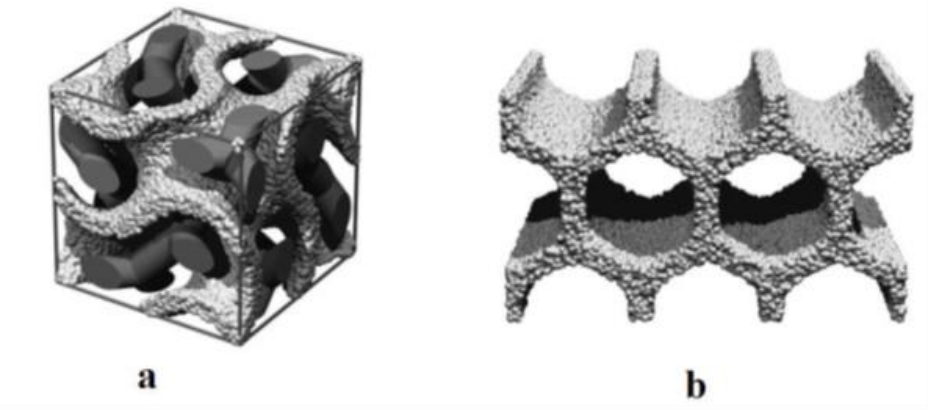

Figure 4: Structure of MCM-48 with template (a) and MCM-41 without template (b)[77]

Chapter 3. Synthesis of T- group particles

3.1 Introduction:

Organosilica materials have always been an interesting research topic because of their organic and inorganic matrices and interactive characteristics. Their promising properties, such as low toxicity, good thermal stability and mechanical strength[81] make them useful in various applications like colloidal photonics crystal,[82] biosensors[83] and in biomedical such as multicolour imaging[84] or an antimicrobial organic coating.[85] So far in the studies on organosilica particles mainly focused on to modified silica surface by using different functional group like vinyltrimethoxysilane (VTMS),[82] methyltrimethoxysilane (MTMS),[86] phenyltrimethoxysilane (PTMS)[87] and mercaptopropyltrimethoxysilane (MerTMS).[88,89] The synthesis of organic/inorganic silica particle is typically carried out with the help of templates[90–92] or emulsion polymerization.[93] These method have various difficulties such as continues implementation of required preliminary steps and the use of several chemicals. As a consequence, the synthesis of organically functionalized silica particles by one-pot synthesis and the replacement of organic solvents by water have recently earned attention.[82,88,89,94]

Up to now in the studies on organosilica particles, several types of nonspherical silica partides have been synthesized like raspberry-like,[95] golfball-like and bowl-like (Scheme 1). Organically functionalized silica particles are formed due to stress shrinking.[96] Meester et al. synthesized silica including crumpled, wrinkled with the rough and smooth surface.[97] Zhou et al made-up hollow organosilica microspheres like golfball-like with wrinkled surface and proposed mechanism based on Ostwald ripening.[86] Yang et al. developed a synthesis of organically functionalised silica particles in aqueous solution in the presence of VTMS and TEOS. By varying the VTMS:TEOS ratio and the ammonia concentration, spherical, golf ball-like or cup-shaped particles are formed.[96] Later there were several mechanism discussed for the synthesis of organosilica porous particles with surfactants and further these silica particles behaved superiorly in the field of drug delivery and cell imaging.[98,99] Whereas Hah et al. prepared monodisperse hollow silica particles without using templates.[100]

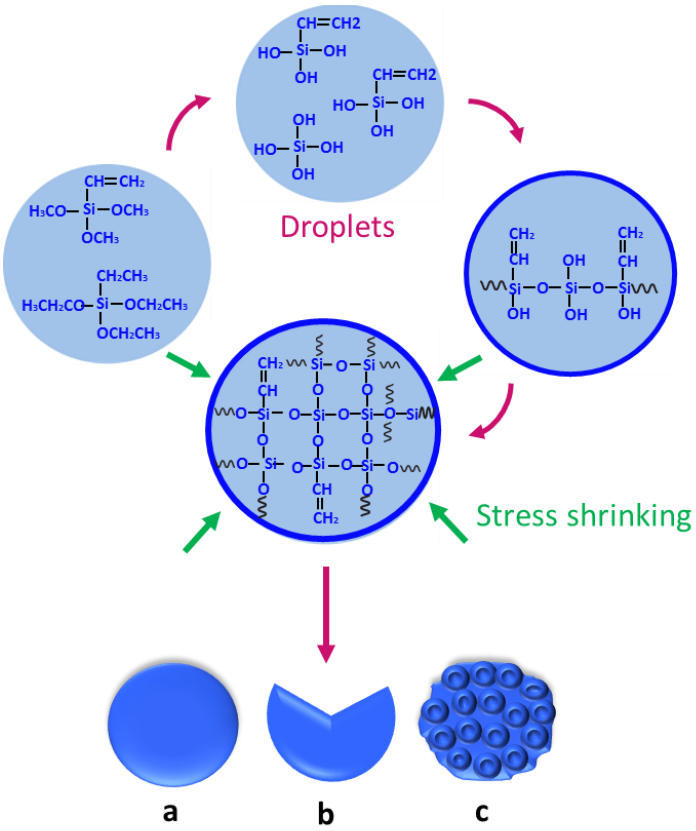

In **Scheme 1**, Product **a), b)** and **c)** describe by the concentration ratio will be controlled from TEOS to VTMS. The sphere particles **(a)** can only be with VTMS,:TEOS with long reaction time, **(b)** an increase in TEOS penetration leads to bowl-shaped particles however, the concentration ratio age of VTMS/TEOS (4:1) golf ball-like particles **(c)**.[96]

According to Yang et al.the formation of the golf ball-like morphology is due to differences in hydrolysis and condensation rates between TEOS and VTMS. With progressive reaction time, the degree of condensation inside the particle successively increases. Consequently, a pressure builds up at the interface of the inner part to the outer part of the particle, which has a higher degree of condensation at the beginning of the reaction. Exceeding the critical pressure value generates the golf ball-like surface.[96]

According to Zhou et al.[86] his theory is based on a core-shell principle with the Ostwald ripening (Scheme 2). Due to the more rapid hydrolysis of TEOS compared to MTMS under identical conditions,[50] aggregates of TEOS form in the first step. MTMS condenses consecutively on the aggregates to polymethylsilsesquioxane. The more hydrophilic inner silica core migrates to

the water phase over time, while the more hydrophobic polymethylsilsesquioxane diffuses into the core to eliminate the high surface energy. During this process, the particle morphology changes from a spherical shape to a golfball-like shape. The conversion to the golfball-like morphology reduces the final particle size. The exclusive condensation of TEOS or MTMS does not generate golfball-like particles. Due to the rapid hydrolysis and condensation of TEOS, small, spherical particles are quickly formed. The hydrolysis and condensation of MTMS produces larger particles compared to the co-condensation of MTMS and TEOS. In the investigation of the synthesis particles from TEOS and MTMS a possible reaction mechanism was discussed. TEOS under basic conditions is faster hydrolysed than MTMS whereby the hydrolysed product of TEOS is converted to silica (SiO_2). This is followed by the hydrolysis and condensation reaction of MTMS to polymethylsilsesquioxane (PMSQ). Here the resulting PMSQ is stored around the previously formed silica particles and forms a core-shell structure. PMSQ is due to its CH_3 residues more hydrophobic than silica and therefore insoluble in water. In view a thermodynamic imbalance arises, which leads to an expansion of the interior. At the same time the migration of polymethylsilsesquioxane takes place inside. This has the consequence that the surface morphology changes from smooth to wrinkle.

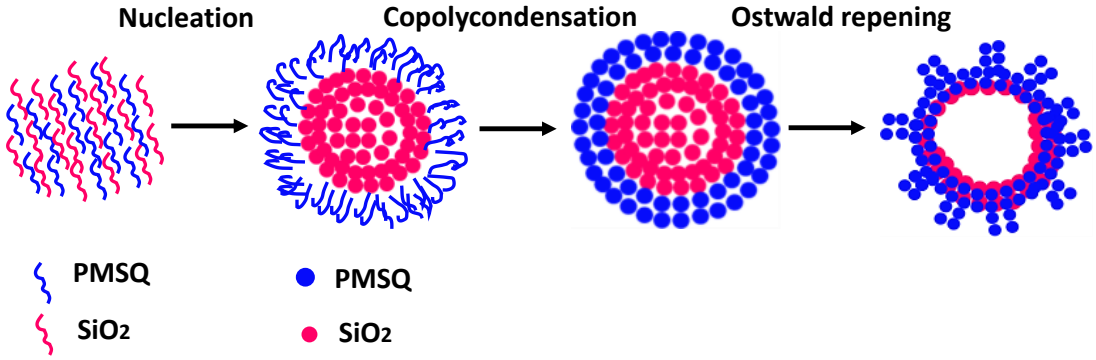

Scheme 2. Mechanism of hollow and wrinkled surface.[86]

Here we describe the mechanism of the formation of a bowl like to spherical monodisperse organosilica particles without using TEOS. The addition of organic solvents, particle size, shape and morphology can be tuned as well as porous particles can form without using templates with the controlled monodispersity. These are unique features of this work. This chapter deals with the synthesis of non-spherical to spherical and nonporous to porous silica particles in the range of 1 µm-5 µm. By the optimization of the synthesis with the variation of feed rate, stirring speed, reaction time and concentration of additives.

3.2 Result and Discussion

Preparation of organosilica particles in micrometre size were performed in a one pot synthesis, where a stirring solution of water and aqueous ammonium hydroxide is added a mixture of the corresponding T group silane; vinyltrimethoxysilane (VTMS), Phenyltrimethoxysilane (PTMS) and 3-mercaptopropyltrimethoxysilane (MerTMS) and optionally tetraethoxysilane (TEOS) and / or an organic solvent over a period of minutes with a syringe pump.

Table 1 Different approaches which were investigated

Source of silanes	Additives	Variations
VTMS	Hexane	Molar concentration of TEOS and silane
PTMS	Toluene	Amount of additives
MerTMS	Mesitylene	Speed of stirring and drop rate of silane
TEOS	*n*-tridecane	Time

3.2.1 Particles V1-V9 made of vinyltrimethoxysilane (VTMS)

3.2.1.1 Influence of the reaction time

This series of experiment was preformed at different reaction times to observe how reaction time influences the size, shape and morphology of the particles. Figure 5 shows the SEM micrographs of the particles **V1**-**V6**, which were generated from VTMS by the variation of reaction time from 50 minutes to 20 hours. Comparing the SEM images of **V1** and **V2** show that within minutes monodisperse, uniform particles are formed with a wrinkled surface morphology. While the particles **V3**-**V6** obtained with long reaction times are showing monodisperse, less wrinkled surfaces and first decreas and then increase again in their size with long reaction time (Figures 5 and 6).

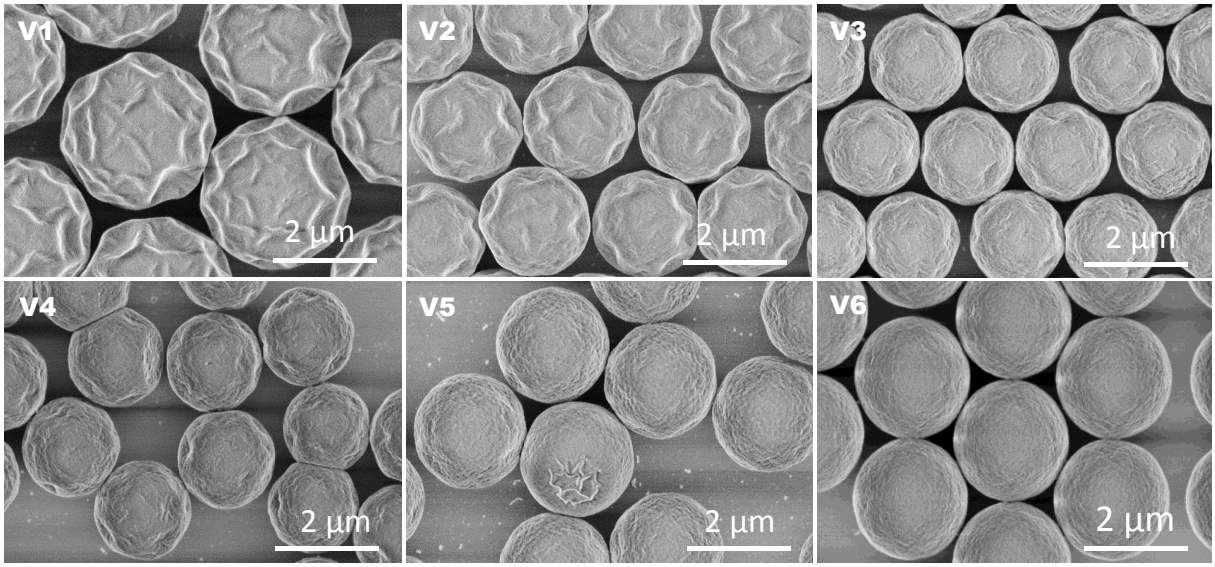

Figure 5: The SEM images of the particles **V1**-**V6** influenced by reaction time.

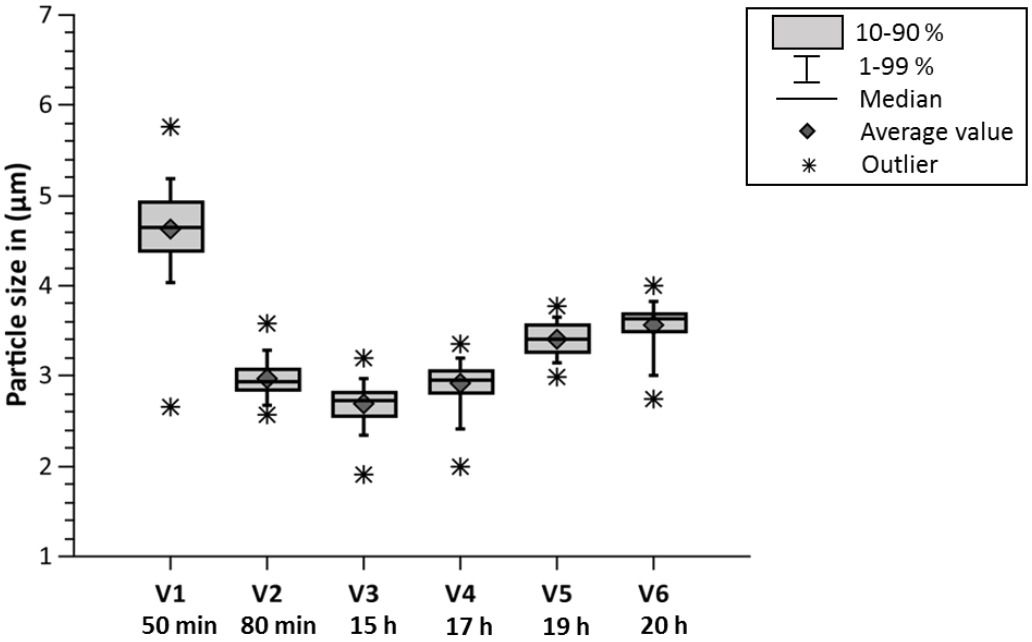

Figure 6: Particle size distribution of **V1-V6** with variation of reaction time.

The box whisker plot in Figure 6 clarifies the distribution of particle size from left to right where **V1** and **V2** generated particles with the diameter of 4.6 µm, 2.9 µm and thus display a significant difference in the particle sizes in a very small time gap. While with increasing reaction time the particles of **V3-V6** were formed with increasing diameter of 2.7 µm, 2.9 µm, 3.4 and 3.6 µm, respectively. With the long reaction time barely any wrinkles are found on the surface, but particles are compressed and decreased in size.

3.2.1.2 Influence of the molar ratio of VTMS and TEOS particles V7-V9

In the following experiments the ratio of the silanes VTMS:TEOS were changed to see the effect on the particles size, shape and morphology. Shown in Figure 7 are the particles **V7**-**V9** synthesized with the molar ratios of TEOS:VTMS of 1:2, 1:1 and 4:1 respectively. Particles **V9** were molded with more TEOS and less VTMS has a huge effect on the surface morphology have been observed. These particles look like bowl-like particles. In the following Images we can see whereas **V8** has greater effect in terms of size whereas **V7** were carrying an equal amount of TESO:VTMS and apart from smooth a surface didn't observe any effect on the surface.

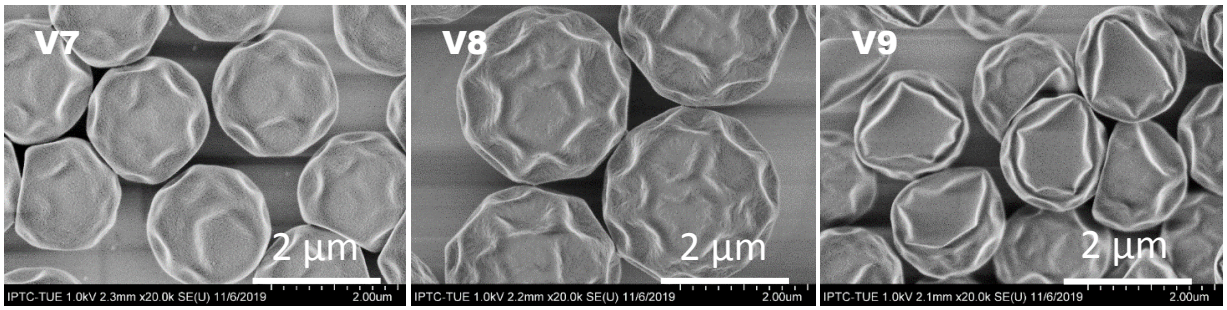

Figure 7: The SEM images of the organosilica particles with different molar ratio. **V7** (1:2), **V8** (1:1), **V9** (4:1).

3.2.2 Particles P1-P18 made of Phenyltrimethoxysilane (PTMS)

The morphology of the organosilica particles are regulated by adjusting the molar ratio of TEOS and PTMS. Particles synthesized with different molar ratios have different sizes and shapes. Figure 8, comparing the SEM images from the molar ratio (**P1a**) 1:4, (**P1b**) 1:2, (**P1c**)

1:1, (**P1d**) 2:1 and (**P1e**) 4:1. It is clearly visible that the particle's surface and morphology drastically changed by changing the molar ratio of silane. Figure 8 **P1a** and **P1e** are showing bowl like particles with one compressed fold in the middle, while for **P1b-P1d** non uniform polydisperse particles are observed and hardly see any shape of the particles.

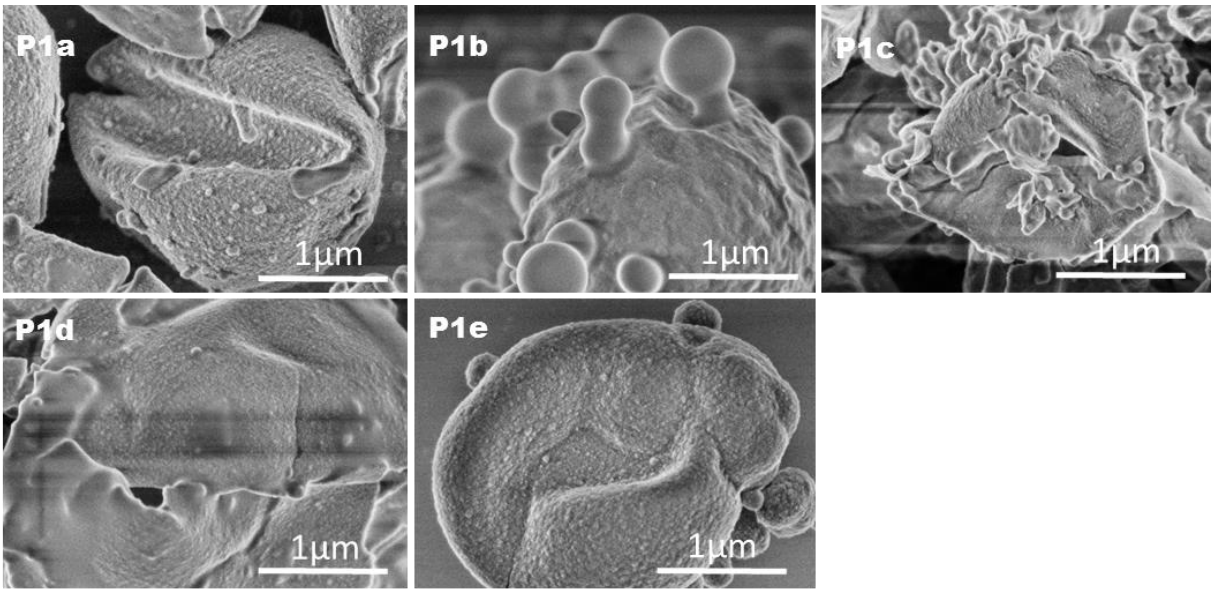

Figure 8: Influence of the silane molar ratio on the morphology and shape of the particles.

General overview of changes in morphology by using different additives in the sol-gel process.

To modify the oil droplet of the T-group various solvents were tested. It was expected that expending the oil drop and dilute/diluting the silane in the droplet should/would generate an effect on the size, morphology and porosity of the particles. Hexane, toluene, mesitylene and *n*-tridecane were added to the increasing size of the droplet.

3.2.2.1 Influence of hexane P3,P5 and P6

In Figure 9 the SEM images of **P3**, **P5** and **P6** are showing the effect of hexane in the droplet during the formation of the particles. **P3** and **P5** show bowl like wrinkled surface particles with a minor difference in particle sizes. These particles were synthesized with the addition of 0.43 ml and 0.7 ml of hexane to the droplet. While **P6** represents monodisperse and spherical particles prepared with 0.86 ml hexane in the droplet. Compared to the morphology of **P3**, **P5** material **P6** is smooth (Figure 9 P6).

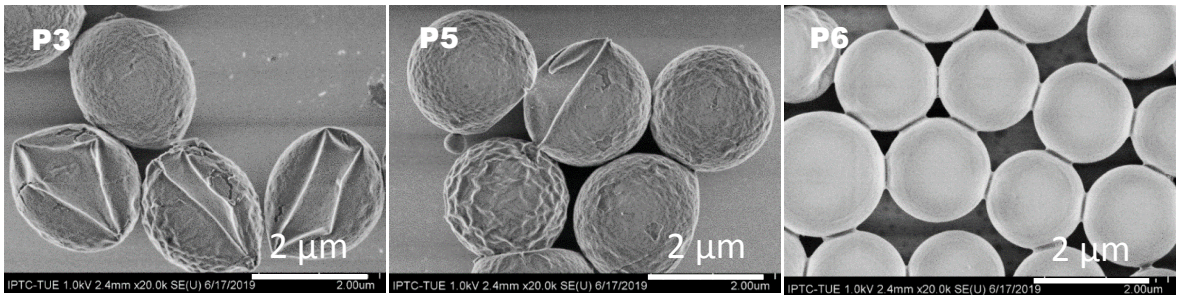

Figure 9 SEM Images of particles **P3, P5** and **P6** influenced by addition of hexane.

Table 2. Variation of hexane on particle morphology and size.

	Hexane	**Size**
P3	0.43 mL	2 µm
P5	0.7 mL	2.1 µm
P6	0.86 mL	1.9 µm

By varying the amount of hexane according to **Table 2** in the synthesis of **P3**, **P5** and **P6** (Figure 10) the size of the particles decreases with increasing the amount of hexane. Particle **P3** and **P5** have a diameter of about 2 µm, 2.1 µm and didn't show much effect on the morphology of the particles. Whereas particles **P6** have a diameter of 1.9 µm with small monodisperse particles. Table 2 and Figure 10, reveals that the particle size can be regulated by varying the addition of solvent while keeping the other process parameters constant.

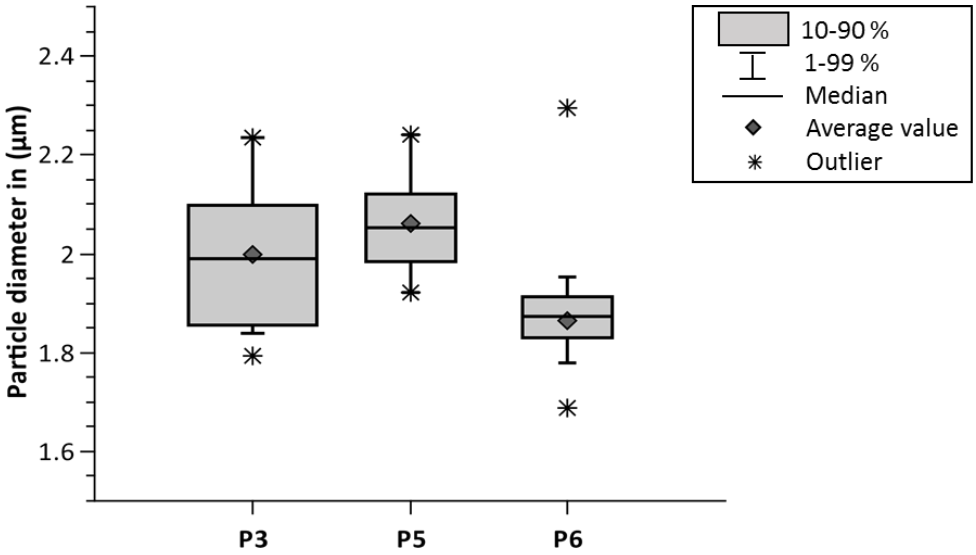

Figure 10 Particle size distribution of **P3**, **P5** and **P6**.

3.2.2.2 Influence of toluene particles P7-P10

In the following increasing addition of toluene was employed (Table 3). The SEM images of the particles **P7-P10**, which were formed with addition of 0.35 ml, 0.59 ml, 0.6 ml and 0.7 ml toluene respectively, can be seen in Figure 11. **P7** and **P8** shows non-uniform polydisperse distributions with wrinkled surfaces; monodisperse smaller particles with smooth surfaces are produced by particles **P9**, **P10**.

Table 3. Variation of toluene on particle morphology and size.

	Toluene	**Size**
P7	0.35 mL	2.3 µm
P8	0.59 mL	2.4 µm
P9	0.6 mL	1.3 µm
P10	0.7 mL	1.5 µm

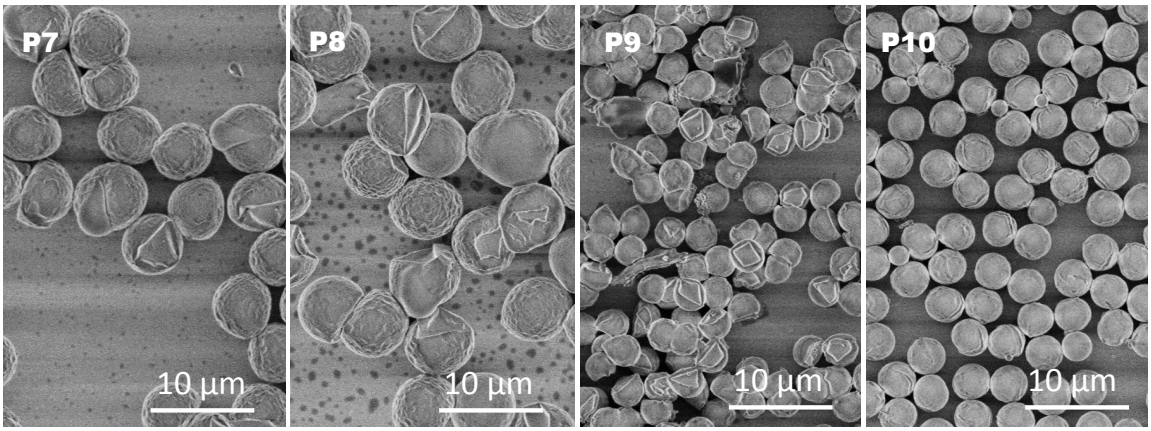

Figure 11: SEM Images of particles influenced by addition of toluene. **P7-P10** respectively.

At lower concentration of toluene can significantly increas the size of the particles. Compared to **P9** and **P10**, **P7** and **P8** provides a larger range of particle size. (See in Figure 11).

3.2.2.3 Influence of mesitylene particles P11-P13

In Figure 12 SEM pictures are illustrating a series of experiments where mesitylene was added to the droplet. The synthesis of **P11**, **P12** and **P14** are performed in a semi-batch Process at 600 rpm. In the micrograph of **P11** it is shown that spherical particles were formed with

wrinkled surfaces while in the case of **P12** and **P13** it is seen that particles were molded from one direction and formed bowl like particles. With the addition of mesitylene, particles have a similar kind of wrinkled surface as well as decreasing order of particle sizes.

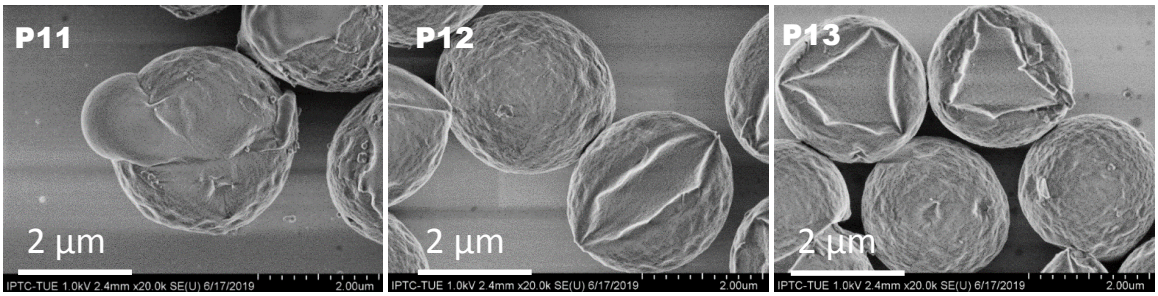

Figure 12: SEM Images of particles **P11-P13** influenced by addition of mesitylene.

Table 4. Variation of mesitylene on particle morphology and size.

	mesitylene	Size
P11	0.46 mL	3.1 µm
P12	0.78 mL	3 µm
P13	1.25 mL	2.5 µm

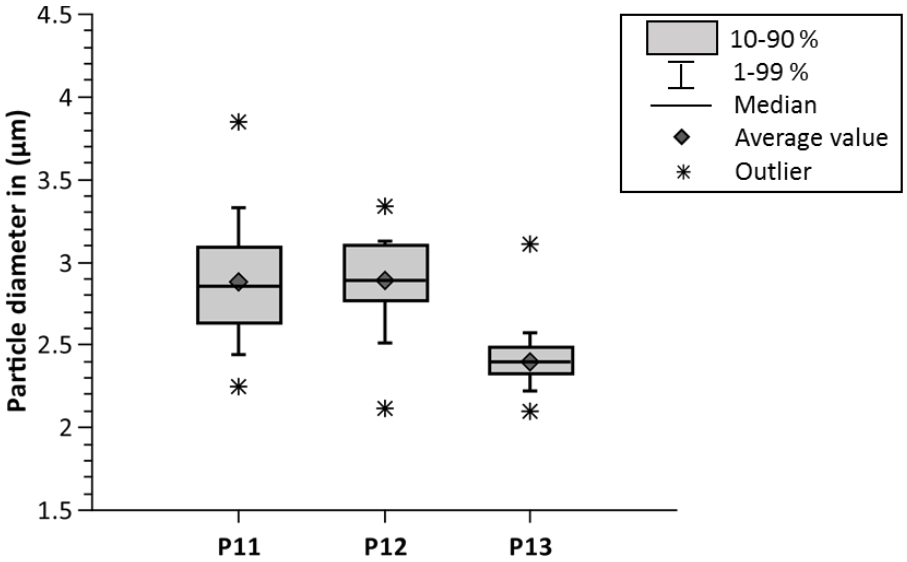

Figure 13: Particle size distribution of **P11, P12 and P13** with mesitylene.

The box plot shows a descending trend in particle size from 3.1 µm to 2.5 µm. The distribution also decreases with an increasingly small amount of mesitylene. It illustrates that the

hydrolysis and condensation reactions have carried out very quickly. Otherwise, no particles of approximately the same size would form. By varying the amount of mesitylene see in.

3.2.2.4 Effect on particles by varying the stirring speed and rate of addition of silane drop

In this study two parameters were compared, varying the stirring speed of the reaction as well as the rate of addition of silane. **P14** is carried out with the stirring speed at 600 rpm, producing particles with a diameter of 2.7 µm.The synthesis of **P15** takes place at a stirring speed of 300 rpm and particles with a diameter of 1.7 µm are produced. With compare the morphology **P14** shows monodisperse, larger particles with wrinkled surface while **P15** displays smaller particles with less wrinkles on the surface. Only in the case of PTMS correlation between stirring speed and particle size confirms that the particle size increases with increasing stirring speed (Figure 14)

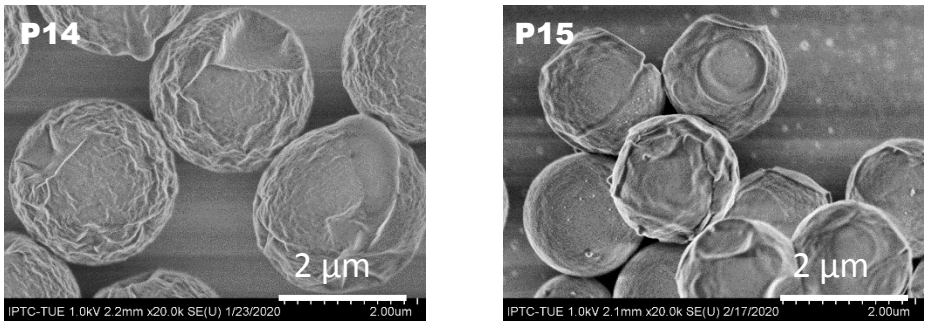

Figure 14: Effect of stirring speed.

As the second parameter, the rate of the addition of silane was varied. In Figure 15F the SEM micrograph of particles **P17** and **P18** are displayed. (prepared at 200 and 600 rpm).With a slow rate of addition (18 mL/h) the spherical, monodisperse particles **P17** with the diameter of 2.4 µm and with the smooth surface are observed. In the case of faster rate of addition (72mL/h), particles **P18** with a diameter of 3.2 µm and a bowl like wrinkled surface are observed.

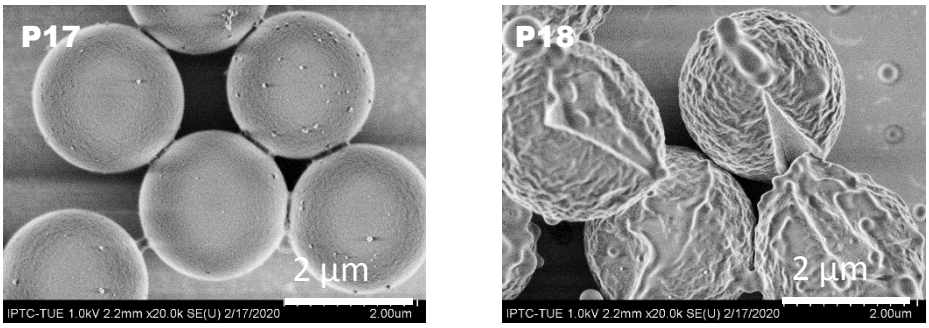

Figure 15: Effect of drop speed.

3.2.3 Particles M1-M28 made of 3-mercaptopropyltrimethoxysilane (MerTMS)

The same approach was used to prepare micron size silica spheres functionalized with 3-mercaptopropyltrimethoxysilane based on the above findings. The variance amount of MerTMS, addition of TEOS and additives were used to develop new particles with controlled size, shape, morphology, and porosity. A time dependent analysis of the particle formation with MerTMS and TEOS was performed and the role of selective additives such as mesitylene, hexane and *n*-tridecane have been discussed. In all conditions, the sizes of these particles was well controlled.

3.2.3.1 Time dependent investigation with TEOS

In this experiment the molar ratio of MerTMS:TEOS was constant. The condensation of TEOS and MerTMS did not generate golfball-like particles and did not have a reasonable effect on the particles **M1**, **M2** and **M3** (Figure 16). Long reaction times formed less dimples on the surface as well as the particle size steadily reduces. There have been few modifications that are noticeable. As seen in **M1** during long reaction time, larger particle displays with wrinkled surface whereas **M2** and **M3** are synthesized in short reaction time, those displaying smaller particle sizes with less wrinkles on the surface (see in Figure 16).

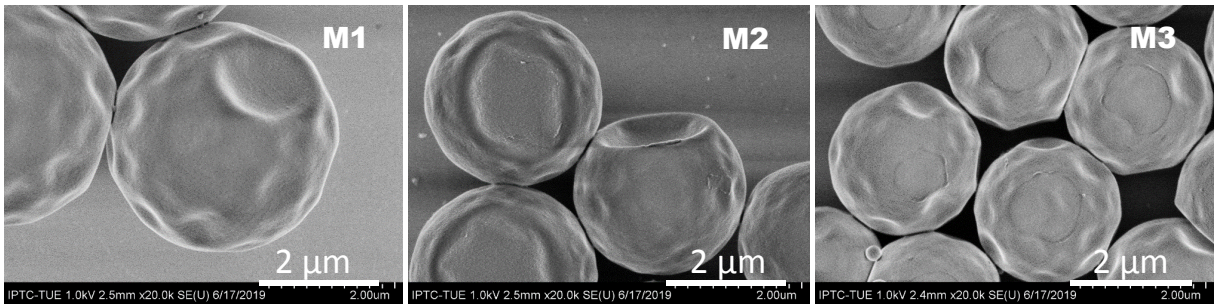

Figure 16: Particles **M1**, **M2** and **M3** Influenced by reaction time.

The particle diameter in the SEM images was randomly measured and corresponding box-whisker diagrams were created in order to better explain the interaction between particle size and reaction time, and then examined their association shown in Figure 17. **M1**, **M2** and **M3** were prepared at 17, 14 and 10 hrs with 3.8, 2.9 and 2.4 µm diameter. Figure 18 shows a noticeable trend is the particle size gradually decreases with decreasing reaction time.

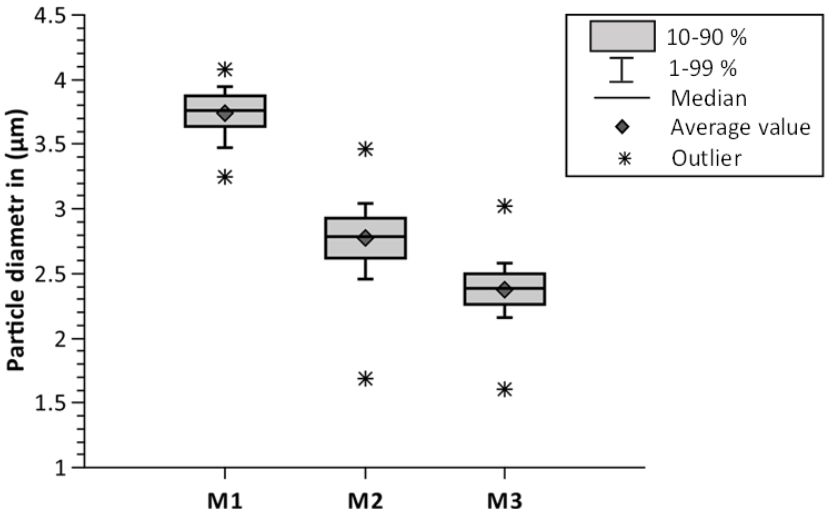

Figure 17: Particle size distribution of **M1**, **M2** and **M3**.

Time-dependent investigation without TEOS but with the addition of mesitylene

In the experiments which were performed here (Figure 18) the reaction time was varied during the formation of MerTMS particles in the presence of mesitylene. Figure 18 shows particles **M4** and **M8** which were formed after 8 and 16 hours while other parameters were constant. Particles **M4** prepared with short reaction time display agglomerated particles but larger in size, whereas particles **M8** generated with long reaction time display monodisperse particles

with a smooth surface but smaller in size. The **M4** display patches on the surface that indicate the agglomeration occurred at the early stage of the reaction while monodisperse microspheres were seen in **M8** with the long reaction time. In both the images particle surface was smooth. Particle diameters of **M4** and **M8** are 3.6 and 1.9 µm.

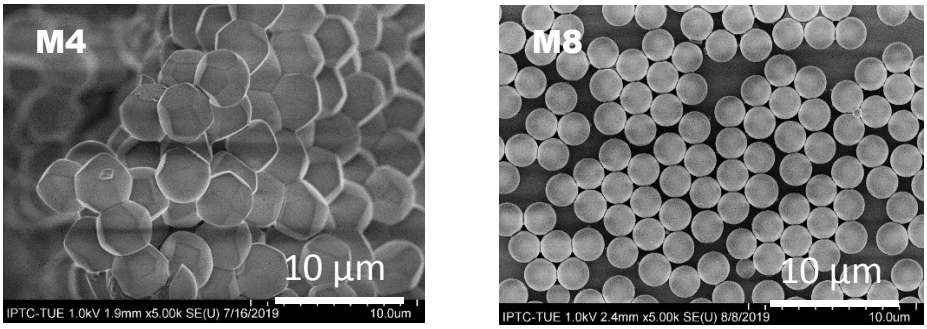

Figure 18: Effect of mesitylene on the particles.

3.2.3.2 Changes in the amount of silanes

In the following, the amount of MerTMS were changed in the presence of mesitylene to see the effect on the particle size,shape and morphology. Particles **M5-M7** shown in Figure 19 were synthesized with the amount of 10.2, 16.4 and 29.4 mL of MerTMS, respectively, while the amount of mesitylene remained constant. Particles **M5** formed with less silanes showed small diameter whereas particles **M6** and **M7** which were formed with more silane showed bigger sizes.

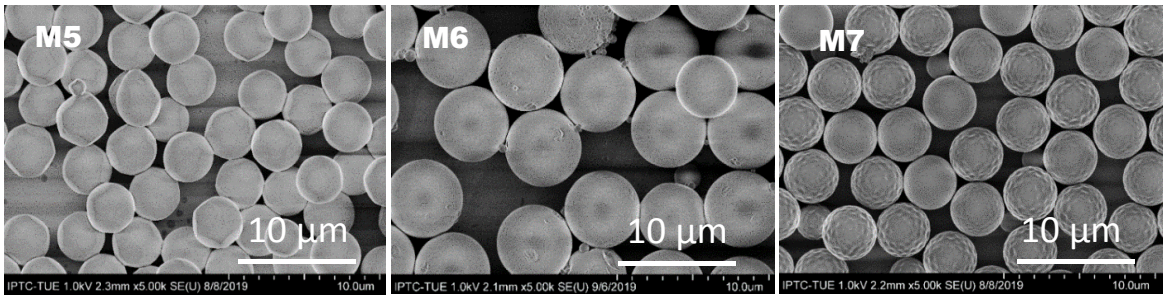

Figure 19: The SEM images of the particles **M5**, **M6** and **M7** influenced by changes in the molar ratio of silane.

In general, the addition of more silane or additives formed larger particle. Figure 20 shows the particle size distribution of **M5**, **M6** and **M7** with diameters of 1.7, 3.7 and 3.5 µm,

respectively. Interestingly, particles **M7** are generated with a larger size distribution compared to **M5** and **M6**.

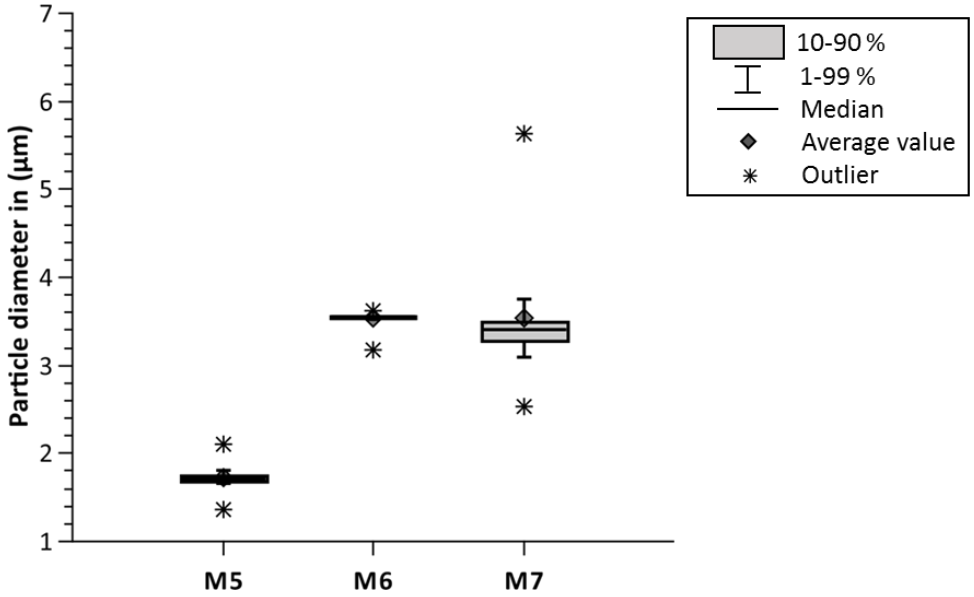

Figure 20: Particle size distribution of **M5**, **M6** and **M7**.

3.2.3.3 Effect of hexane on the growth of particles

Particles **M9** to **M12** were synthesized with the addition 0.3, 0.4, 0.6, and 2.4 ml of hexane respectively (Figure21,Table 5). In the cases of **M9** and **M10** with only small amounts of hexane the microparticles aggregate. Interestingly on the surface of **M19** small granules were observed. Whereas with a high addition of hexane, monodispersed particles were formed with smooth surfaces (Figure 21).

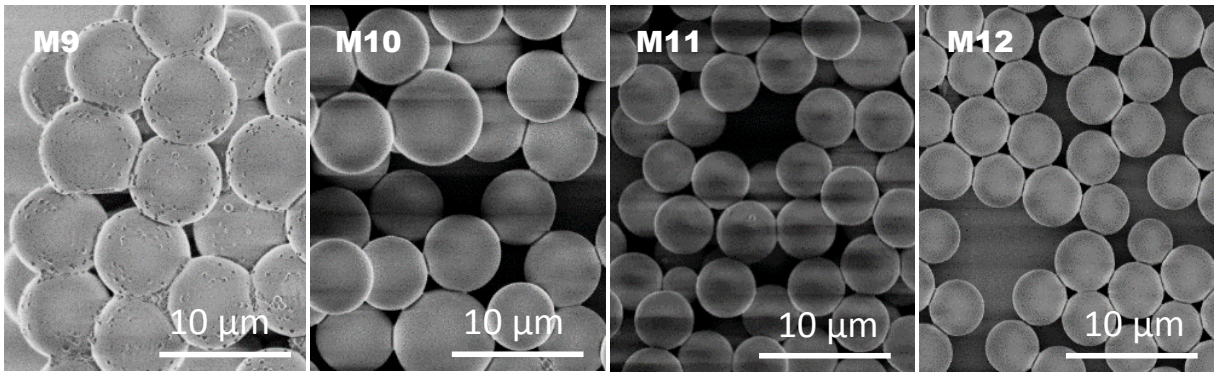

Figure 21: Particles influenced by amount of hexane.

Table 5. Variation of hexane on particle and size

	Hexane	Size
M9	0.3 mL	4.4 µm
M10	0.4 mL	3.8 µm
M11	0.6 mL	2.7 µm
M12	2.4 mL	2.9 µm

The diameter of the particles **M9**-**M12** of 4.4, 3.8, 2.7 and 2.9 µm were obtained from their box-whisker plots (Figure 22). The particles **M12** display the narrowest size distribution with small diameters. Thus use of high amounts of hexane is responsible to the formation of smaller monodisperse particles.

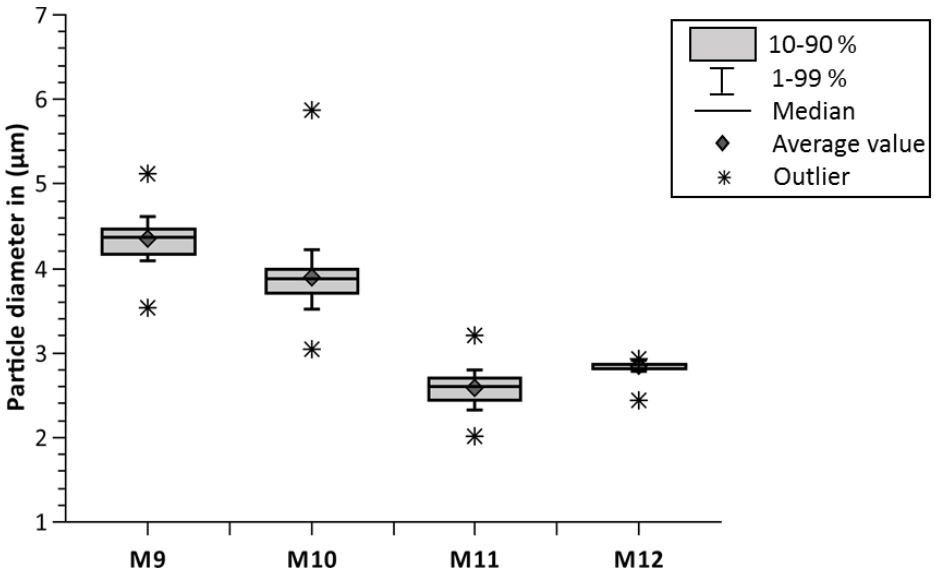

Figure 22: Particle size distribution of particle **M9**, **M10**, **M11** and **M12** influenced by different amount of hexane.

3.2.3.4 Effect of *n*-tridecane

After mesitylene and hexane the role of *n*-tridecane as additive in the MerTMS oil droplets was investigated.

Figure 23 displays particles **M13**, **M14** which were formed with an addition of *n*-tridecane while other parameters remained constant resulting in huge differences in the surface morphology, size and porosity. In particle **M13** higher amount 5.47 mL of *n*-tridecane were used and shows a smooth surface with large particle diameter 2.5 µm in size, whereas **M14**

were formed with the addition of 2.7 mL of *n*-tridecane and monodisperse porous particles with a diameter 1.9 µm were observed.

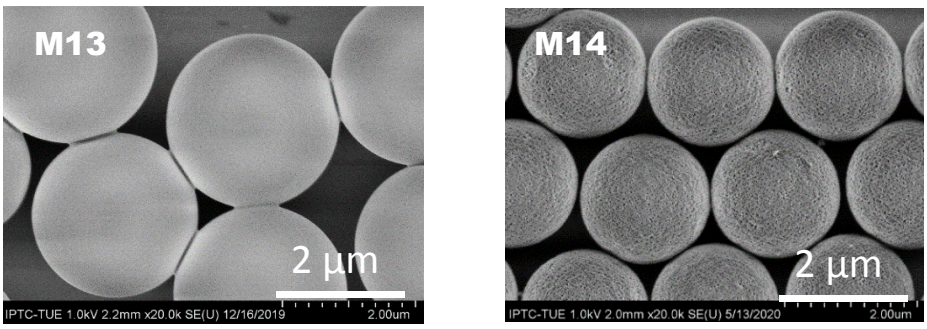

Figure 23: Effect of *n*-tridecane**.**

3.2.3.5 Role of n-tridecane on the particle size and porosity.

The *n*-tridecane concentration has been discussed here for the preparation of highly porous organosilica particles functionalized with MeTMS. Figure 24 showing the SEM micrographs of the particles **M15**-**M22** which were prepared by the addition of *n*-tridecane. The effect on the particle size and porosity was investigated due to variation of *n*-tridecane. In this reaction condition, when the amount of *n*-tridecane was adjusted in the range from 1.31-3 mL (Table 6) mesoporous organosilica particles were obtained (Figure 24). The porosity and surface area were characterized by BET analysis (see in Figure 28). Figures 24 and 25 show that particle size increased continuously as *n*-tridecane concentration increased from 1.31 to 2.7 mL. Further addition of *n*-tridecane has no effect on the particles size.

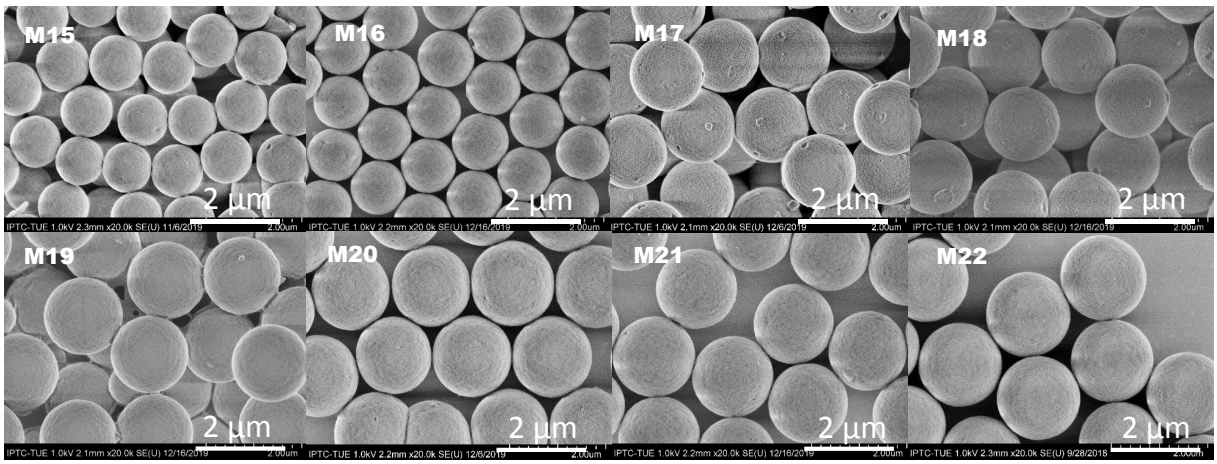

Figure 24: Size influences due to variation of *n*-tridecane

Table.6 Variation in concentration of *n*-tridecane

	MerTMS	*n*-tridecane	Diameter in (µm)
M13	20.4 mL		2.7
M14	20.4 mL	2.7 mechanical Stirring	1.9
M15	20.4 mL	1.31 mL	1
M16	20.4 mL	2 mL	1.2
M17	20.4 mL	2.5 mL	1.4
M18	20.4 mL	2.6 mL	1.5
M19	20.4 mL	2.7 mL	1.6
M20	20.4 mL	2.8 mL	1.7
M21	20.4 mL	2.9 mL	1.7
M22	20.4 mL	3 mL	1.7

In order to evaluate the monodispersity and size of the particles, 100 random particles were chosen to determine their size distribution by SEM. These data clearly showed that the size of the particles increased with increasing amount of *n*-tridecane (Figure 25).

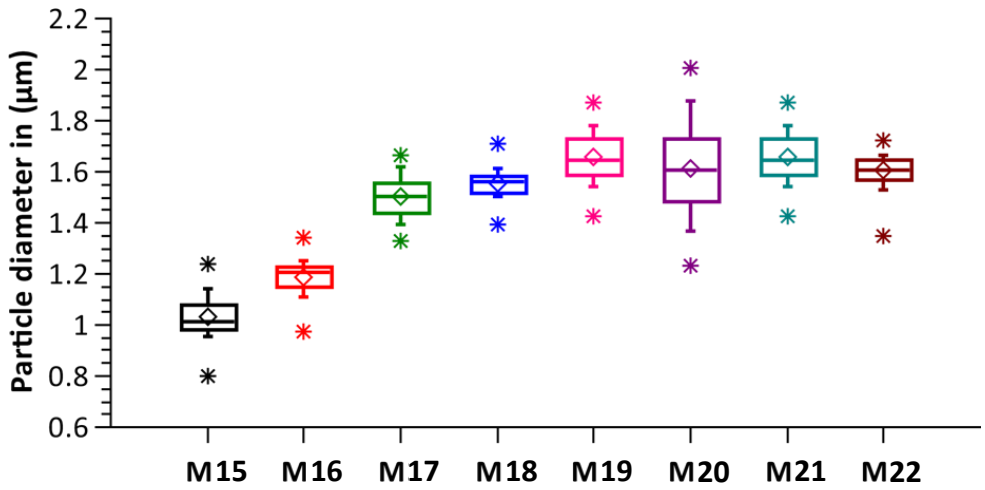

Figure 25: Concentration of the *n*-tridecane influenced size of the particles.

3.2.3.6 Control the morphology and porosity by using mechanical stirrer

There was another method used to form porous silica microspheres by using a mechanical stirrer. The particles **M23**-**M25** shown in Figure 26 were synthesized with the addition of 2.5, 2.7 and 3 mL *n*-tridecane and 8 hours of reaction time. In all cases monodisperse porous particles were formed. As shown in Figure 26 the particles **M23** and **M24** which were synthesized with less amount of *n*-tridecane have smooth surfaces and diameters of 1.52 and 1.57 µm while particle **M25** formed with more *n*-tridecane had a ruptured surface morphology with the diameter 1.4 µm in size.

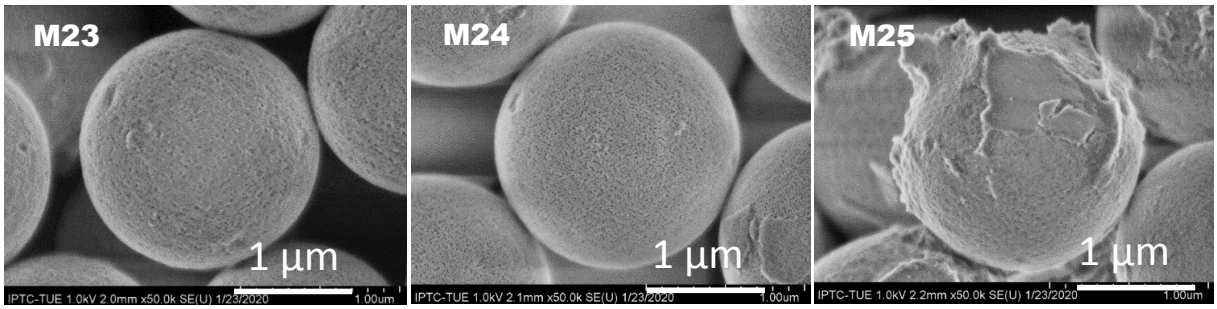

Figure 26 Representative effect on the morphology, size and porosity of the particles with less reaction time by using mechanical stirrer.

In contrast particles **M26**, **M27** and **M28** were also obtained by using a mechanical stirrer with long reaction time (16 hours) rest parameters remained similar as **M23**-**M25**. With long reaction time particles increased in size also in porosity but at particular condition. In Figure 27 the particle **M26** was observed smaller in size with less porosity as compared to **M27** and **M28**, those were observed larger in size with high porosity.

The morphology of the particles **M26**-**M28** could be readily adjusted by controlling the concentration of *n*-tridecane and reaction time.

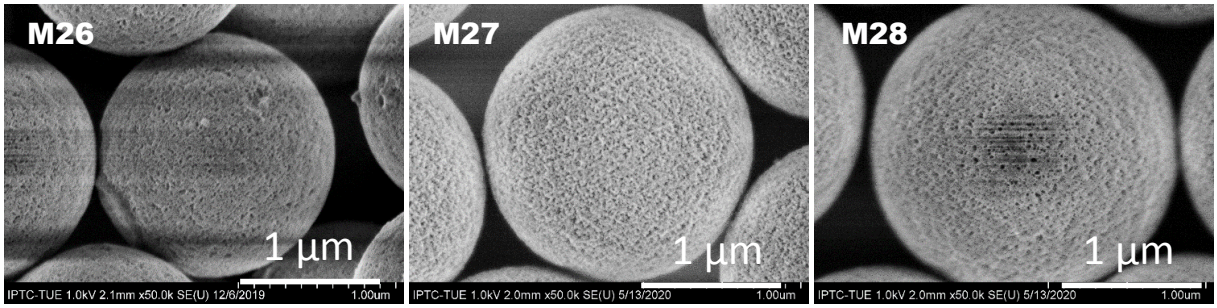

Figure 27 Illustrating the effect on the porosity and size of the particles with long reaction time by using mechanical stirrer.

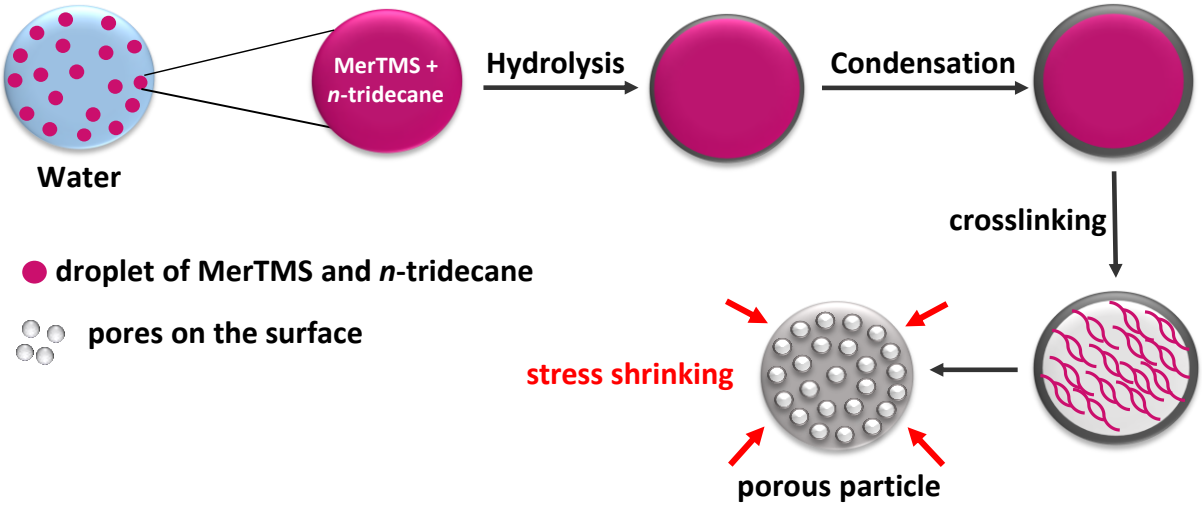

Scheme 3. The reaction mechanism of the particles functionalized by MerTMS an addition of *n*-tridecane.

3.2.3 Physisorption

Reversible nitrogen adsorption and desorption isotherms are found for the materials **M27** and **M28** which displays a typical Langmuir IV hysteresis (Figure 28).[101] The H1 loop is characteristic for narrow uniform mesopores[101,102] as found in MerTMS silica particles. The average pore size calculated from the adsorption branch of the nitrogen isotherms by the BJH method (Table 7) ranged from 5.3 to 6.7 nm. Interestingly, stirring for were observed.

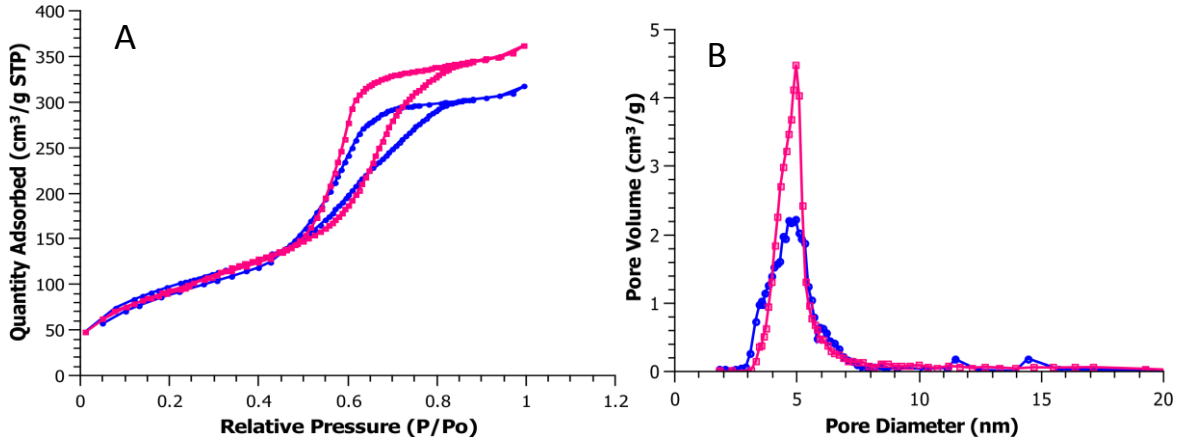

Figure 28: Nitrogen Adsorption and Desorption Isotherms (**A**) and BJH Pore volume and pore diameter (**B**) for **M27** (●) and **M28** (■)

Table 7. Pore size distribution and specific surface area obtained by nitrogen physisorption of **M27** and **M28**.

	Pore volume [cm^3/g^{-1}]	Surface area [m^2/g]	Pore size [nm]	Particle diameter [µm]
M27	0.55	334	5	1.8
M28	0.47	368	5.2	1.6

3.2.4 Characteristion of particles

The particles genrated from PTMS and MerTMS are characterised by DRIFT, ^{13}C and ^{29}Silica solid state NMR spectroscopy.

Representative DRIFT spectra of the phenyl and mercapto particles are shown in Figures 29 to 31. Particularly characteristic vibration ranges are shown in Table 8. The absorption band found in $1000 - 1200\ cm^{-1}$ corresponding to valence vibration of Si-O-Si groups. The Si-C_6H_5

groups can be clearly assigned by the bands at $700\ cm^{-1}, 740\ cm^{-1}, 1430\ cm^{-1}$ and $1593\ cm^{-1}$. The phenyl ring can be characterized by the aromatic C-H valence oscillations above $3000\ cm^{-1}$. The FTIR spectrometer is also able to assign the bands of the terminal Si-OH deformation oscillation at δ=$918\ cm^{-1}$. In addition, Si-OH groups, a strong and wide band occurs at $3624\ cm^{-1}$.

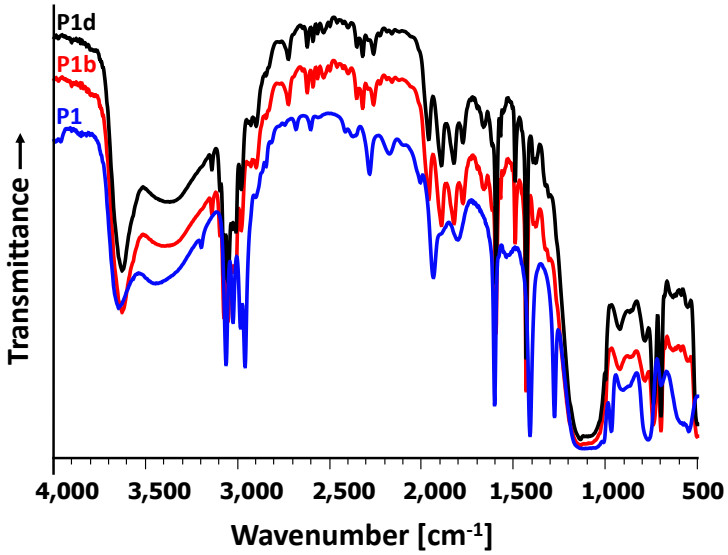

Figure 29: DRIFT spectra of the materials **P1**, **P1b**, and **P1d** in comparison with the different molar ratio pf silane.

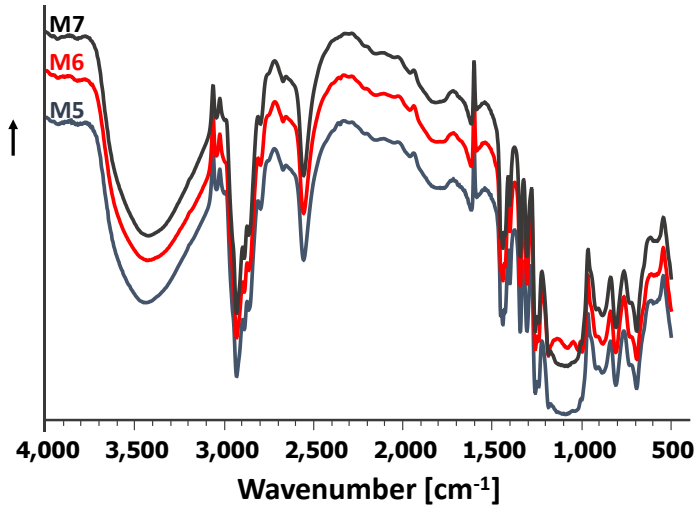

Figure 30: DRIFT spectra of the materials **M5**,**M6**.and **M7** in comparison with the different amount of silane.

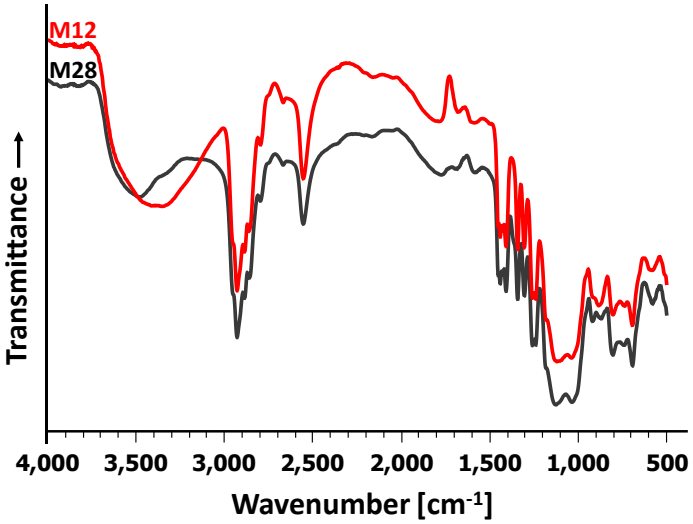

Figure 31.a: DRIFT spectra of the materials **M12** and **M28** in comparison with the addition of hexane and *n*-tridecane.

From the spectrum it can be seen that these different silica particles are the cross-linked products resulting from the hydrolysis and condensation of PTMS, and the addition of organic low molecular weight solvents maintains the original structure.

Table 8. Classification of Absorption bands

Wavenumbers in [cm^{-1}]	**Vibrations**
3600	ν (OH)
3500-3000	Various ν (OH)
3000-2900	ν (CH_2), ν (CH_3)
2554	ν (H-S)
1600	ν (C=C)
1400	δ (C=C)
1300	δ (CH)
1200-1000	ν_{as} (Si-O-Si)
950	ν (Si-OH)
800	δ (O-Si-OH)
600	ν_s (Si-O-Si)
450	δ (O-Si-O)

In the ^{13}C solid state NMR spectra of the VTMS, PTMS and MerTMS particles characteristic resonances for the vinyl (Figure 32), phenyl (Figure 33 and mercapto (Figure 34) functions are observed.

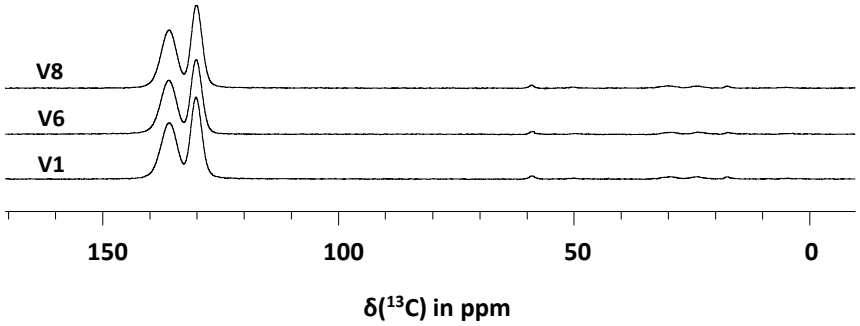

Figure 32: Representative ^{13}C-NMR spectra (CP/MAS) of the vinyl particles **V1**, **V6** and **V8**

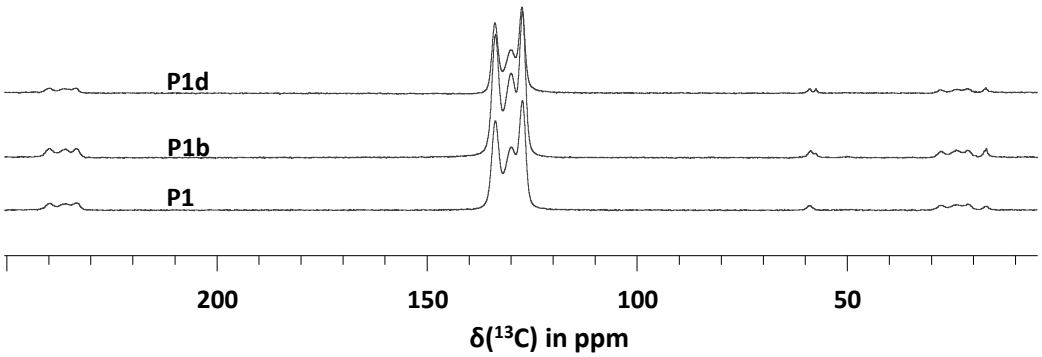

Figure 33: Representative ^{13}C-NMR spectra (CP/MAS) of the vinyl particles **P1**, **P1b** and **P1d**.

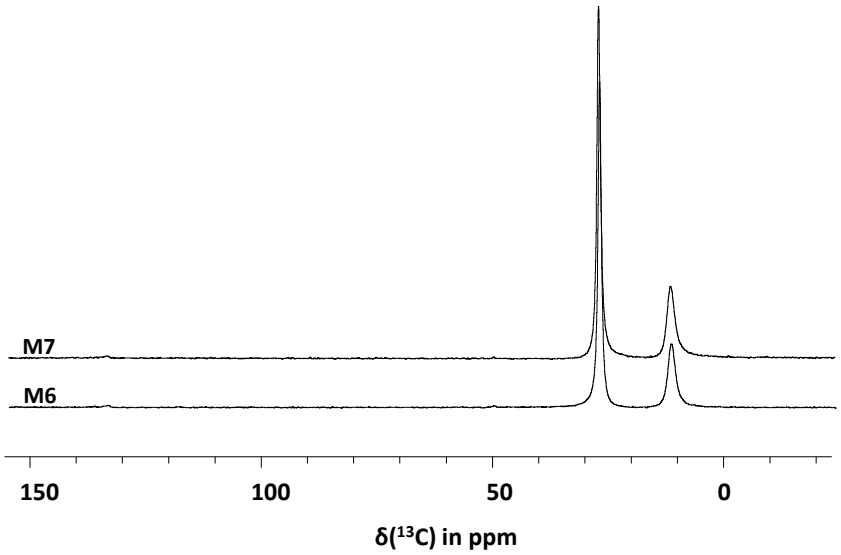

Figure 34: Solid state ^{13}C-NMR spectra (CP/MAS) of the particles **M6** and **M7**

In the ^{29}Si solid state NMR spectra of the VTMS, PTMS and MerTMS particles characteristic resonances for T^2 and T^3 groups (Figures 35 and 36) are found. In those cases where TEOS was applied as additive Q groups were found as well.

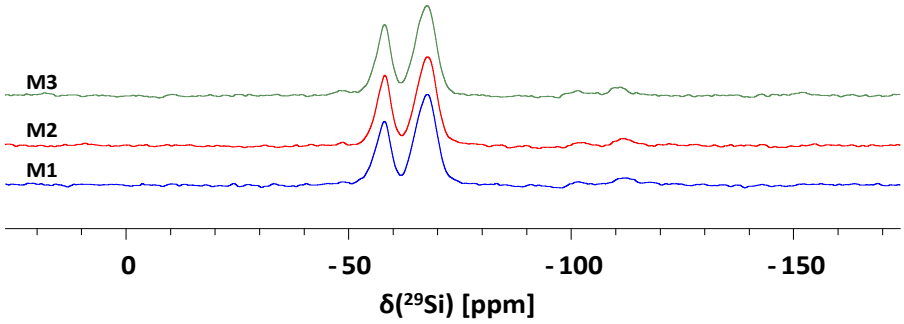

Figure 35: Solid-state ^{29}Si NMR spectra (CP/MAS) of the compared particles **M1**, **M2** and **M3**.

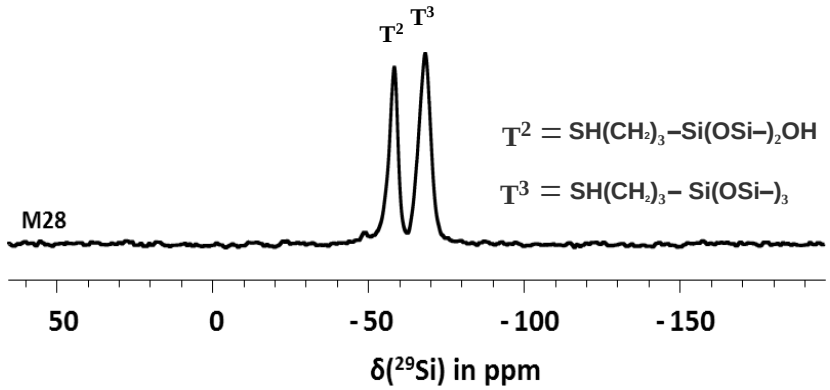

Figure 36: Solid-state ^{29}Si NMR spectra (CP/MAS) of the particles **M28**.with of *n*-tridecane.

3.5 Conclusion

The oil in water emulsion technique was applied to produce organic inorganic hybrid materials. The shape, size, surface morphology, and porosity strongly depend on the organic function of the T-group silane precursor and the reaction conditions, like stirring speed and reaction time. Additives like TEOS or organic molecules like hexane and *n*-tridecane further allow to fine tune characteristic features of the particles.

Based on the evaluation of the results presented here and those reported earlier following mechanism of the formation of the particles is proposed. The precursors, consisting of VTMS, PTMS and MerTMS are insoluble in water and form small oil droplets, which are distributed in the water under strong stirring. As ammonia as a catalyst dissolves in the water those silane precursors which are located on the surface of the droplets would first start to hydrolyse and condense. The hydrolysed product groups are hydrophilic, vinyl, phenyl and 3-mercapto groups are hydrophobic in nature. The hydrolysed silanes are distributed on the surface of the oil droplets. Consequently, the condensation of the Si-OH groups takes place on the boundary surface between the oil-water interface, forming a cross-linked organosilica network immediately on the surface of oil drop. Thus a skin of a silane network is formed around the droplet. As water and catalyst diffuse through the porous skin the frontline of hydrolysis and condensation moves from the outside to the inside of the droplet and the viscosity of the skin increases with increasing thickness. The hydrolysis and condensation within the droplet has two further consequences. As T-groups are applied three moles of alcohol per T-group are generated. Second, the formation of Si-O-Si bonds from two Si-OR units leads to a reduction of the volume of the final silica material. This shrinking process leads to a pressure on the silica particle. When the critical value of structural stability is exceeded, the particles deform, to escape the stress and then form a wrinkled surface while methanol and ethanol is released to the water. Due to the different rates of hydrolysis and condensation of VTMS, PTMS, and MerTMS there are some differences in the degree of networking during the process between the exterior and the interior of the organosilica particles. Interestingly use of different silanes particles were formed with different morphology, shape and size and porosity. With VTMS golfball-like particles were observed, while with PTMS bowl-like particles with one cut in the middle were obtained, and with MerTMS particles greater in size, as well as the porous surface, was observed.

Chapter 4. Synthesis of core-shell dumbbell silica particles with simultaneous drug delivery

4.1 Introduction:

Mesoporous materials with multilevel morphology and hierarchical pore structures have been developed.[72,103–106] Such particles provide different compartments and phase separated domains and are thus interesting candidates for multi drug delivery purposes.[107–109] Moreover the amphiphilic character, which is often accompanied by such multifunctional particles, increases the interfacial activity which improves the particle cell interaction.[110]

Recently anisotropic dumbbell core-shell silica microparticles, that are composed of two different hemispheres (Figure 37) were prepared.[111] The two lobes differ in size so that the particles are shaped like dumbbells, snowmen or acorns.[112] The shells of both lobes are constructed of mesoporous MCM-41 type channels and differ in their thickness. On the surface of the large lobe many SiOH functions were replaced by Si-F groups. Consequently, the surface charge of the smaller hemisphere is more negative than that of the larger hemisphere which gives the particles an amphiphilic character. While the core of the large lobe is dense, the interior of the small hemisphere is hollow. Thus, three compartments can be identified: (i) the shell of the large lobe with a weak surface charge, (ii) the shell of the small lobe that is negatively charged and (iii) the hollow cage that is covered by the small hemisphere. The diversely functionalized hemispheres (SiF vs SiOH) as well as the different compartments make these particles attractive materials for the co-delivery of multiple drugs with different properties and functions.

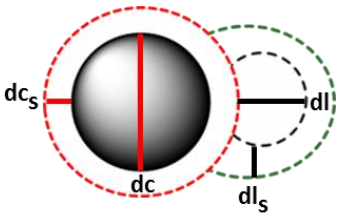

dc = dumbbell core
dcs = dumbbell core shell
dl = dumbbell lobe
dls = dumbbell lobe shell

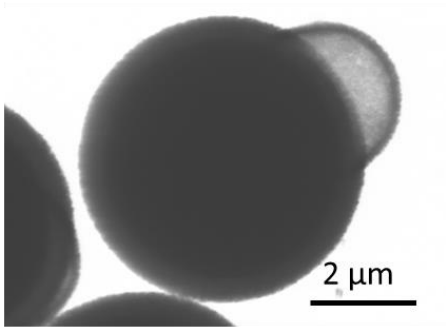

Figure 37. Cartoon of the anisotropic, amphiphilic core-shell dumbbell particle (dl, dl_s, dc and dc_s: diameter and thickness of the hollow cavity and its shell as well as of the dense core and its shell, respectively)

Although several studies have highlighted the controlled release of various therapeutic agents with mesoporous silica particles,[113–115] in most of the reported examples only one kind of drug is entrapped into the mesoporous silica materials.[116] Up to date, the co-delivery of multiple drugs with different molecular properties remains difficult.[117] However, the possibility to load and release different drugs on the same systems allows to combine therapies and increases the opportunities for treating diseases. This co-delivery requires materials with the ability to load and release drugs with different properties and functions.

The natural polyphenols curcumin (Cur) and quercetin (QT) affect numerous cellular targets and show activity on the cellular level.[118–123] Both compounds suffer from poor bioavailability due to their low solubility in aqueous solutions and low stability in a biological environment. Consequently, several approaches to deliver both natural polyphenols with different types of drug carriers have been suggested.[124–131]

4.2 Results and discussion

4.2.1 Synthesis of CS1, CS2, DCS1, DCS2, DCS3 and DCS4 microparticles

The protocol of the recently reported one-pot synthesis of monodisperse dumbbell silica core-shell particles was applied to prepare the **CS1**, **CS2, DCS1, DCS2, DCS3** and **DCS4** particles (Figure 38 and 39).[111] To this end, a homogeneous suspension of nonporous dense spherical silica particles (d = 1.5 µm), CTAB and *n*-tridecane was treated under stirring with a water solution of ammonia/ammonium fluoride at 90°C. Stirring below 190 rpm generated the spherical core-shell particles **CS1 and CS2** (Figure 38 a-b, g-h), while stirring between 210 and 240 rpm produced the amphiphilic dumbbell particles **DCS1-3** (Figure 39 c-e,i-k). If the ammonium fluoride is replaced by ammonium carbonate the **DCS4** particles (Figure 39 f,l and Table 9) were obtained. In this etching process,[4,116–118] silica species are gradually dissolved from the surface of the dense silica particles and re-condensed close to the site of dissolution.[32] In cooperation with the CTAB micelles, which are located on the surface of the silica particles, these silica species generate MCM41 type, mesoporous shells around the silica particles.[132] Due to the addition of the swelling agent *n*-tridecane, additional droplets formed that adsorbed on the surface and served as templates for the formation of the second hemispheres in **DCS1**-**DCS4** (Figure 39).

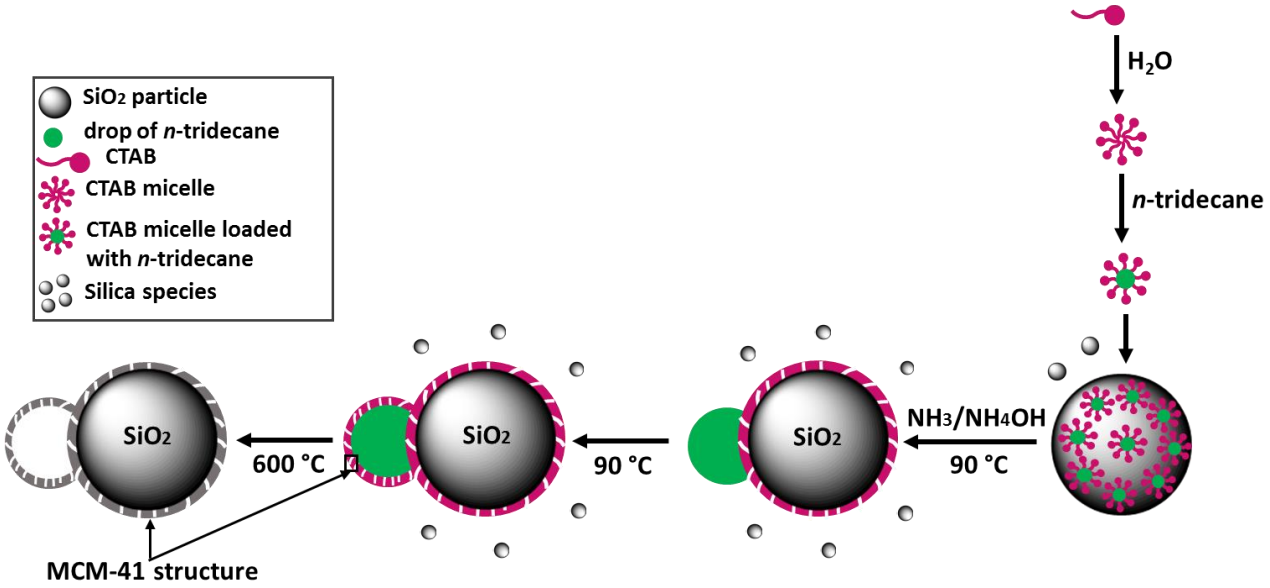

Scheme 4: Proposed mechanism for the formation of the MCM-41 structure and core-shell dumbbell silica particles.

Table 9. Experimental conditions of the **CS** and **DCS** silica particle synthesis

	$m(SiO_2)$ [g]	$V(H_2O)$ [mL]	$V(NH_4OH)$ [mL]	$n(NH_4F)$ [mmol]	V(*n*-tridecane) [mL]	reaction time [h]	stirrer	stirring speed [rpm]
CS1	2.1	210	12	2.38	22	24	mechanic	210
CS2	2.1	210	12	1.35	50	24	mechanic	210
DCS1	2.1	210	12	1.35	60.1	24	mechanic	240
DCS2	2.1	210	12	1.35	50	16	mechanic	250
DCS3	2.1	210	12	2.02	75	43	mechanic	170
DCS4	7.0	700	40	-2	38.7	24	anchor	210

-2 Instead of 4.86 mmol NH_4F, 4.86 mmol $(NH_4)_2CO_3$ was used.

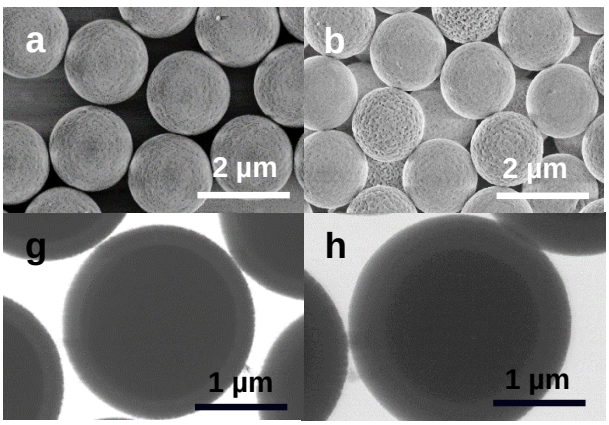

Figure 38: SEM images of **CS1 and CS2** (a, b), **STEM** (g, h) of silica particles.

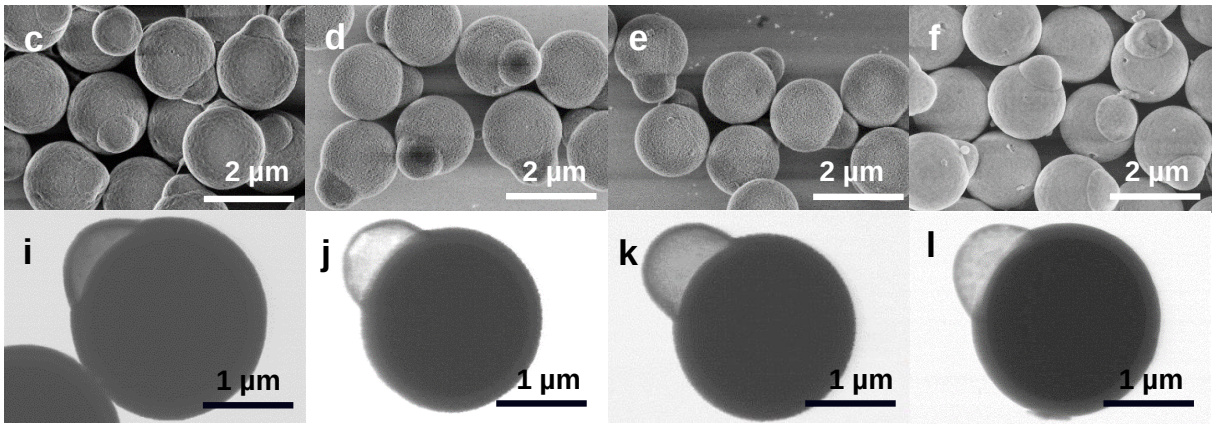

Figure 39: SEM (c-f) and STEM (i-l) images of **DCS1** (c,i), **DCS2**(d,j), **DCS3**(e,k) and **DCS4** (f,l) silica particles.

4.2.3 Characterization of the particles

According to the SEM and STEM micrographs, the protocol produces monodisperse spherical **CS1**, **CS2** (Figure 38 a,b,g,h) and dumbbell like anisotropic particles **DCS1, DCS2, DCS3** and **DCS4** (Figure 39 c-f,i-l). The core and the shell as well as the hollow cavity of the small hemispheres in **DCS1** to **DSC4** can be distinguished from the STEM micrographs (Figure 39 i-l and Table 8). The shells that cover all particles consisted of highly hexagonally ordered tunnels with uniform pore sizes of approximately 4.3-5.9 nm (Figure 39, Table 10). The thickness of the mesoporous shell of the spherical **CS1, CS2** was 176 ,316 nm and can be adjusted with the reaction time.[101] Changing in reaction time, a shell as thick as 139, 118 , 121 and 124 nm around the dense cores in **DCS1**-**DCS4** were formed. The shells of the small hemispheres, which cover the hollow cavity, were 53, 66, 74 and 47 nm thick, respectively (Table 10).

Table 10. Pore size distribution and specific surface area obtained by nitrogen physisorption of **CS1, CS2** and **DCS1-4**. Geometrical parameters dc, dc_s, dl and dl_s (for definition see Figure 38)

	Specific surface area (m^2/g)	Total pore volume (cm^3/g)	Average pore size (nm)	dc (nm)	dc_s (nm)	dl (nm)	dl_s (nm)
CS1	239	0.32	4.3, 5.7	1230	176		
CS2	192	0.26	4.6, 5.1	1171	316		
DCS1	118	0.18	4.8, 6.1	1446	139	189	53
DCS2	121	0.17	4.2, 5.3	1359	118	362	66
DCS3	107	0.19	4.6, 5.8	1325	121	379	74
DCS4	201	0.30	4.5, 5.9	1220	124	340	47

Reversible nitrogen adsorption and desorption isotherms are found for the core-shell materials **CS1, CS2** and **DCS1**-**DCS4**, which display a typical Langmuir IV hysteresis (Figure 40).The H1 loop is characteristic for narrow uniform mesopores as found in template MCM-41 silica.[102] The average pore size calculated from the adsorption branch of the nitrogen isotherms by the BJH method (Table 10) ranged from 4.3 to 5.9 nm. Interestingly, for **CS2** and **DCS3** bimodal pore distributions within this range were observed.[101] All physicochemical data of the anisotropic core-shell particles compare well with those reported for dumbbells of this type.[111]

Interestingly, the only dumbbell particle **DCS4** is generated by the RC1e reaction calorimeter (Thesis of Björn Brodbeck, University Tübingen 2020) compared to the **CS1, CS2** and **DCS1-3** particles synthesized with the mechanical stirrer (Table 9). Average pore size distributions calculated from the adsorption branch of the nitrogen isotherms by the BJH method (Table 10) range from 4.5nm to 6.7nm. All physicochemical data of the anisotropic core-shell particles compare well with those reported for dumbbells of this type.[111] The remaining relevant reversible nitrogen adsorption desorption isotherms and pore size distributions are shown in (Figure 40).

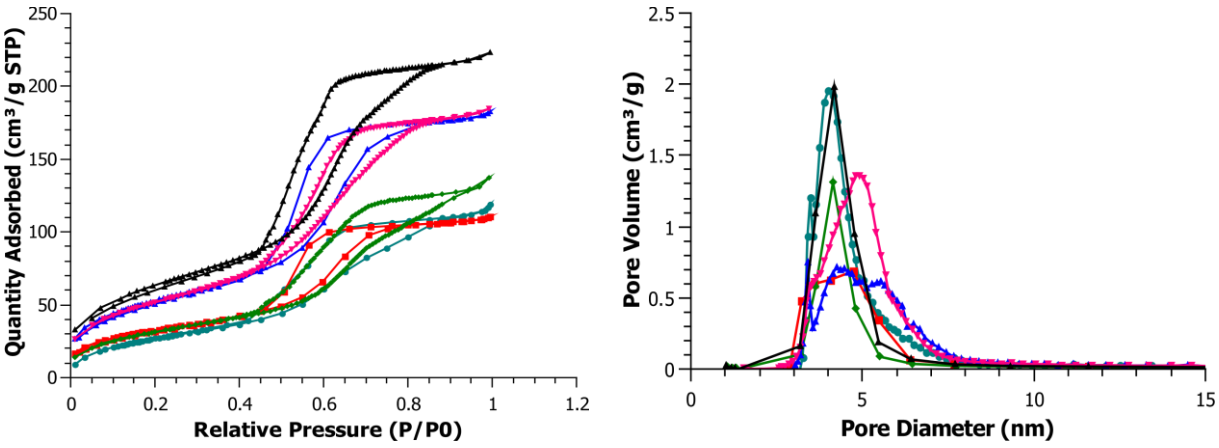

Figure 40: Nitrogen Adsorption and Desorption Isotherms (**a**) and BJH Pore volume and pore diameter (**b**) for **CS1** (▲), **CS2** (▼), **DCS1** (◀), **DCS2** (◆), **DCS3** (■) and DCD4 (●)

Dying experiments with positively and negatively charged dyes of the rhodamine family demonstrated the amphiphilic character of the anisotropic particles **DCS1** (Figure 39).[111] The different zeta potentials on the smaller and larger lobe were traced back to the exchange of surface SiOH groups with SiF functions on the larger hemisphere.[111] This is a consequence of

the application of NH_4F as etching agent. Introducing ammonium carbonate as etching agent generated the anisotropic dumbbell particles **DCS2** with a uniform charge distribution across the particle surface. This finding agrees with an overall smaller Zeta potential for **DCS2** (-47.4 ± 0.9 mV) than for **DCS1** (-25.5 ± 0.6 mV). Compared to the spherical **CS** and anisotropic **DCS2** particles, the amphiphilic dumbbells **DCS1** have smaller specific surface areas and smaller pore volumes.

The amphiphilic properties of the anisotropic dumbbell particles (**DCS3**) were demonstrated with negatively and positively charged dyes (**Figure 42** a-c). **DCS3** was coloured with a positive charged dye (Alexa Fluor® 514, **Figure 42** a) and a negative charged dye (sulforhodamine B, **Figure 42** b), respectively, and with both dyes simultaneously (**Figure 42** c). Alexa Fluor® 514 accumulates in the hollow cavity of the dumbbell particle, while sulforhodamine B accumulates on the core-shell particle. This discrimination is induced by the use of ammonium fluoride as etching agent. Ammonium fluoride substitutes SiOH by SiF on the surface of the silica particle. This leads to a decrease of the negative charge on the particle. The semi-sphere of the dumbbell particle consists exclusively of silica and is consequently negatively charged. Ammonium carbonate as an etching agent provides a uniform negative charged surface on the **DCS4** particles. The dyeing of the **DCS4** particles with the positively charged dyes atto 488 amine (green) and rhodamine 6g (red) leads to an equal accumulation of both dyes on the main particle and the semi-sphere (Figure 41 d and e), respectively.

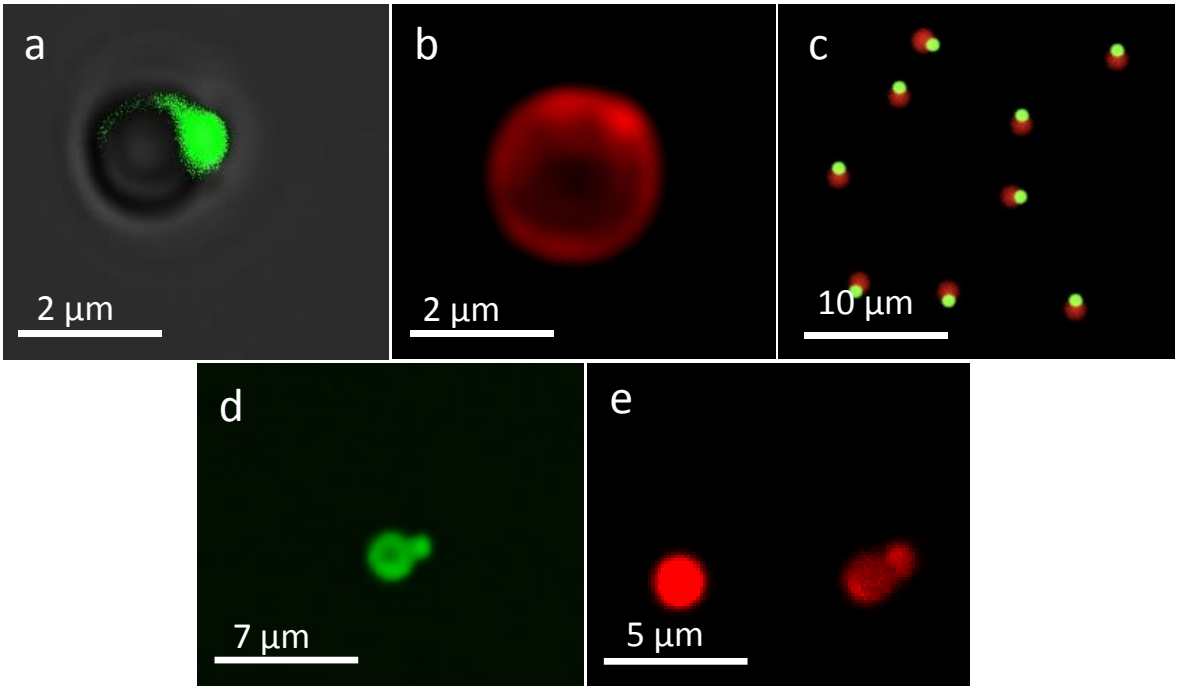

Figure 41: **DCS3** coloured with (a) positively charged alexa fluor® 514 (green), (b) negatively charged sulforhodamine B (red) and (c) with negatively charged sulforhodamine B (red) and positively charged alexa fluor® 514 (green); **DCS4** coloured with positively charged (d) atto 488 amine (green) and e) rhodamine 6g (red)

This assumption is confirmed by zeta potential measurements. The zeta potential decreases, if ammonium carbonate is used (**DCS4**, -47.4 ± 0.9 mV) instead of ammonium fluoride (-25.25 ± 0.6 mV) as etching agent.

4.2.4 Drug loading efficiency

In general, the amount of drug that can be loaded onto mesoporous silica depends on the surface area, the pore volume, the pore geometry and on the number of silanol groups on the surface, which when deprotonated are responsible for the negative surface charge of the silica material. This dependency is nicely reflected in the drug loading efficiency of the spherical **CS2**, the anisotropic and amphiphilic **DCS1-3** as well as the anisotropic and non-amphiphilic **DCS4** particles when treated with ethanolic solutions of equimolar amounts of both drugs Cur and QT. As summarized in Table 9, the overall loading behaviour of Cur plus QT is similarly high but varies widely between Cur and QT among these five types of particle.

While comparable loading contents were found for Cur (45 ± 5 %) and QT (43 ± 6 %) in mesoporous **CS2**, the anisotropic and amphiphilic **DCS1-4** loaded larger amounts of Cur than QT, **DCS1 Cur** (53± 6%) and QT (36 ± 2%), **DCS2 Cur (**55± 5%) and QT was (38 ± 3%) **DCS3** loaded larger amounts of Cur (58 ± 6%) than QT (40 ± 7 %) (Table 11). There was even a more pronounced difference of Cur and QT loading in the anisotropic and non-amphiphilic partide **DCS4**. For these particles, 85 ± 6 % loading efficiency of Cur and only 10 ± 5 % for QT were observed. This difference is remarkable since **CS2** and **DCS4** provide comparable specific surface areas and total pore volumes (Table 10). Contrary to this, although the total pore volume of the dumbbell particle **DCS3** was much less compared to that of the **CS2** particle (Table 10), the overall loading efficiency of Cur plus QT in **DCS3** was even higher than in **CS2** (Table 11).

Table 11. Drug loading efficiency of **CS2**, **DCS1**, **DCS2**, **DCS3** and **DCS4**

	Cur loading efficiency [%]	QT loading efficiency [%]	Total drug loading [%]
CS2	45 ± 5	43 ± 6	88 ± 11
DCS1	53 ± 6	36 ± 2	89 ± 8
DCS2	55 ± 5	38 ± 3	93 ± 8
DCS3	58 ± 6	40 ± 7	98 ± 13
DCS4	85 ± 6	10 ± 5	95 ± 11

From the molecular point of view, these results can be explained in terms of the interaction of Cur and QT with the surface Si-OH and Si-F functions, respectively. Both polyphenols are able to interact with Si-OH groups on silica surfaces. The keto-enol tautomerism of Cur supports donating as well as accepting hydrogen bonds.[119,133] However, under the present reaction conditions it is assumed that Cur interacts with its enolic form with the nucleophilic Si-OH groups on the silica surface of the particles.[134] Consequently, Cur prefers to accumulate in those areas of the particles with negative zeta potentials. In contrast to this QT selects a more lipophilic environment when forming adducts with surface Si-OH groups.[135] Thus, QT is stored in areas with non-polar Si-F functions. Because the spherical core-shell particles **CS** contain Si-OH and Si-F functions, which are equally distributed over the whole surface both drugs are loaded in comparable amounts into the mesoporous shell (Table 11). In **DSC2**, only

Si-OH groups are uniformly spread across the anisotropic particle making it more attractive for Cur than for QT.

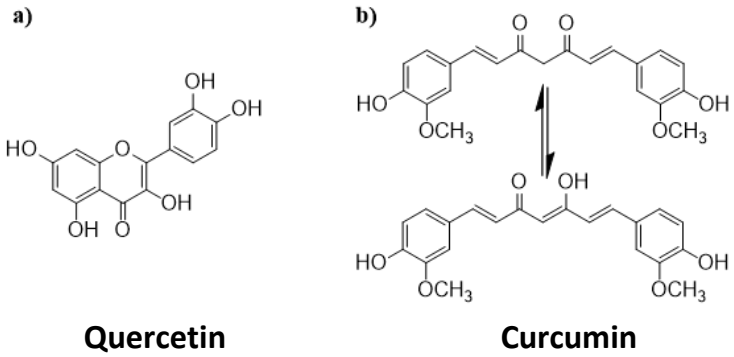

Quercetin **Curcumin**

Figure 42. Chemical structure of a) quercetin, b) Keto/enol tautomerism of curcumin.

Most interestingly, the amphiphilic character of **DSC1** allows QT to be loaded into the porous shell of the large lobe and most of Cur into the porous shell of the small hemisphere. Moreover, the hollow cavity of the small hemisphere in **DCS1** serves as a compartment for Cur as well. This is deduced from the large amount of Cur loaded in **DCS1** compared to the small shell of the small lobe (Tables 10 and 11). Thus, the mesoporous channels in the shell of the small lobe allow the diffusion of Cur into the cavity.[136] The permeability for small molecules of the shell covering the cavity has been demonstrated earlier.[111] This indicates that if both Cur and QT are loaded at the same time to **DCS1** they encapsulate into different areas of the silica particle. This hypothesis is supported by confocal Raman microscopy (Figure 43).

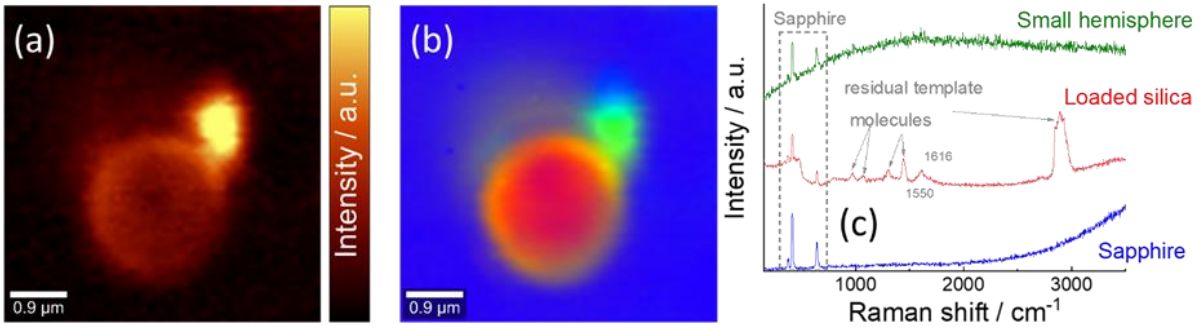

Figure 43: a) Raman intensity distribution image of Cur-QT-**DCS1** in the spectral range 150 cm^{-1} to 3500 $cm^{-}1$; b) Intensity distribution of the Cur-QT-**DCS1** of three components based on a Principle Component Analysis (PCA); c) the corresponding spectra for each component.

Figure 43a shows the Raman peak intensity distribution across a silica particle of **DCS1** loaded with Cur and QT in the spectral range from 150 cm^{-1} to 3500 cm^{-1}. The particle is clearly distinguishable from the background; it shows a medium intensity in the area that can be associated with the core-particle and a much higher intensity in the region of its small hemisphere. A principle component analysis (PCA) of all Raman spectra yielded three principle components explaining 93 % of the total data. Based on this number of responsible components, the data were further analysed (see Methods). For better visualisation, the components were assigned to different colours (blue, red, green). The result of the deconvolution is shown in Figure 43b. The blue component can be associated with the substrate (sapphire), the red with the core-particle and the green with the lobe of the small hemisphere. The shell of the large lobe is yellow indicating a coexistence of the two components (green, red). The corresponding spectra are shown in Figure 43c.

The spectrum of the blue component is dominated by the signals from sapphire with prominent peaks at 412 cm^{-1}, 645 cm^{-1} and 312 cm^{-1}; the increasing background from 2500 cm^{-1} is also typical for sapphire.[137]

The spectrum of the red component shows a number of peaks. Besides the prominent peaks of sapphire, typical signals from silica and residual template molecules are also present at 969 cm^{-1}, 1073 cm^{-1}, 1305 cm^{-1}, 1444 cm^{-1} and a broad peak at 2893 cm^{-1}. This peak can be assigned to residual template molecules in the pores of **DCS1** since a spectrum was measured with and without drugs loaded (Figure 44). The remaining peaks at 1550 cm^{-1},

$1616\ cm^{-1}$ can be assigned to the loaded drugs. The assignment was not straight forward due to the strong overlapping of the signals in this region. The peak at $1616\ cm^{-1}$ and $1550\ cm^{-1}$are close to C=O stretch and O-H bend of QT respectively.[138] Nevertheless, certain peaks of Cur also appear in the same range e.g. C=O stretch at $1626\ cm^{-1}$ and C=C aromatic stretch at $1601\ cm^{-1}$.[139–142] However, Cur should show a luminescence which was not observed in this contribution. Also, its prominent peak at $1626\ cm^{-1}$ is missing. The green component is dominated by luminescence without additional Raman peaks. This luminescence peak can be attributed to Cur since the fitting results showed a maximum at approximately $1500\ cm^{-1}$ that corresponds to 578 nm. This wavelength is close to the fluorescence emission of Cur.[143,144] In conclusion, QT prefers to load into the shell of the large lobe while Cur was in the shell and in the cavity of the small hemisphere. Note that accumulation of minor amounts of Cur on the large lobe cannot be excluded.

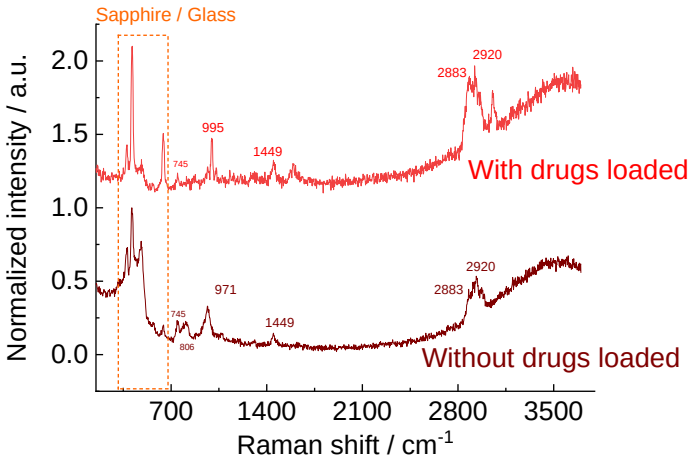

Figure 44. Comparison between Raman spectra of the **DCS1** particles with drugs loaded andwithout drugs loaded.

4.2.5 In vitro drug release study

The drug release behaviour for Cur and QT loaded **CS2**, **DCS3** and **DCS4** particles were evaluated at pH 5.5 and 7.4 (Figure 45). As the Cur loading content was higher in **DCS3** and **DCS4**, the percentage of drug release was also higher than that of QT in the dumbbell particles. All particles showed quicker drug release at acidic pH. Both drugs got released faster from the dumbbell particles **DCS3** (6 h) and **DCS4** (7 h) than from the spherical **CS2** (9 h) mesoporous particles in the acidic environment. At physiological pH, Cur was released faster than QT from all particles (Figure 45).

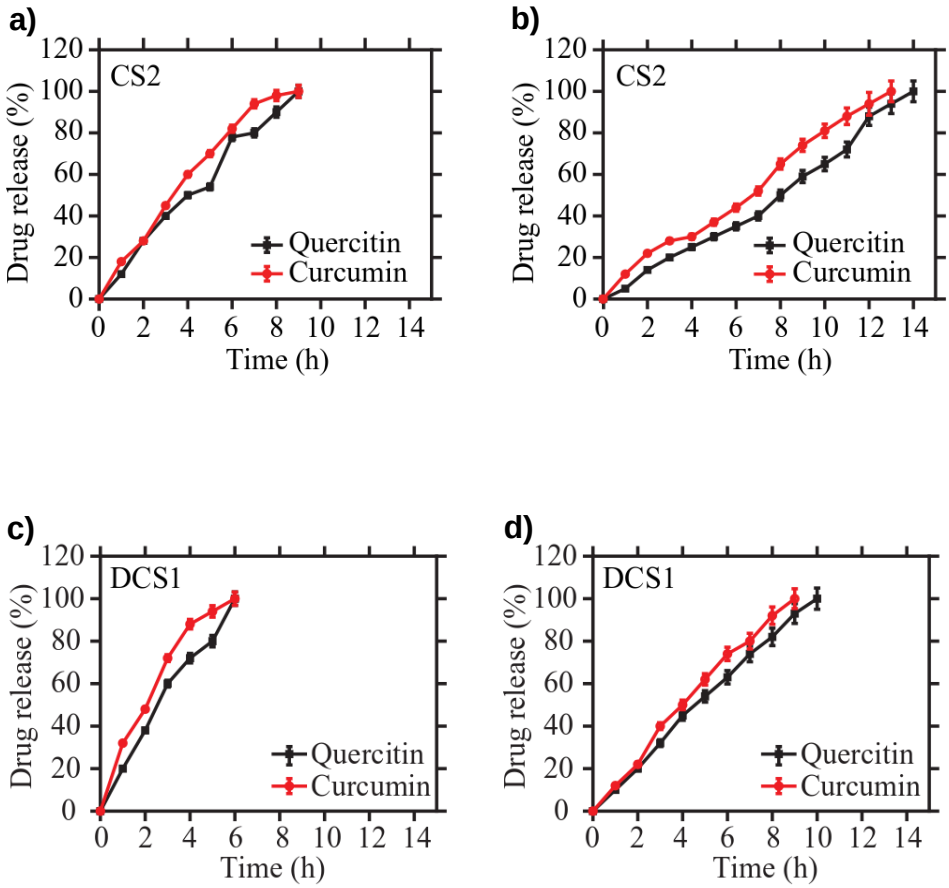

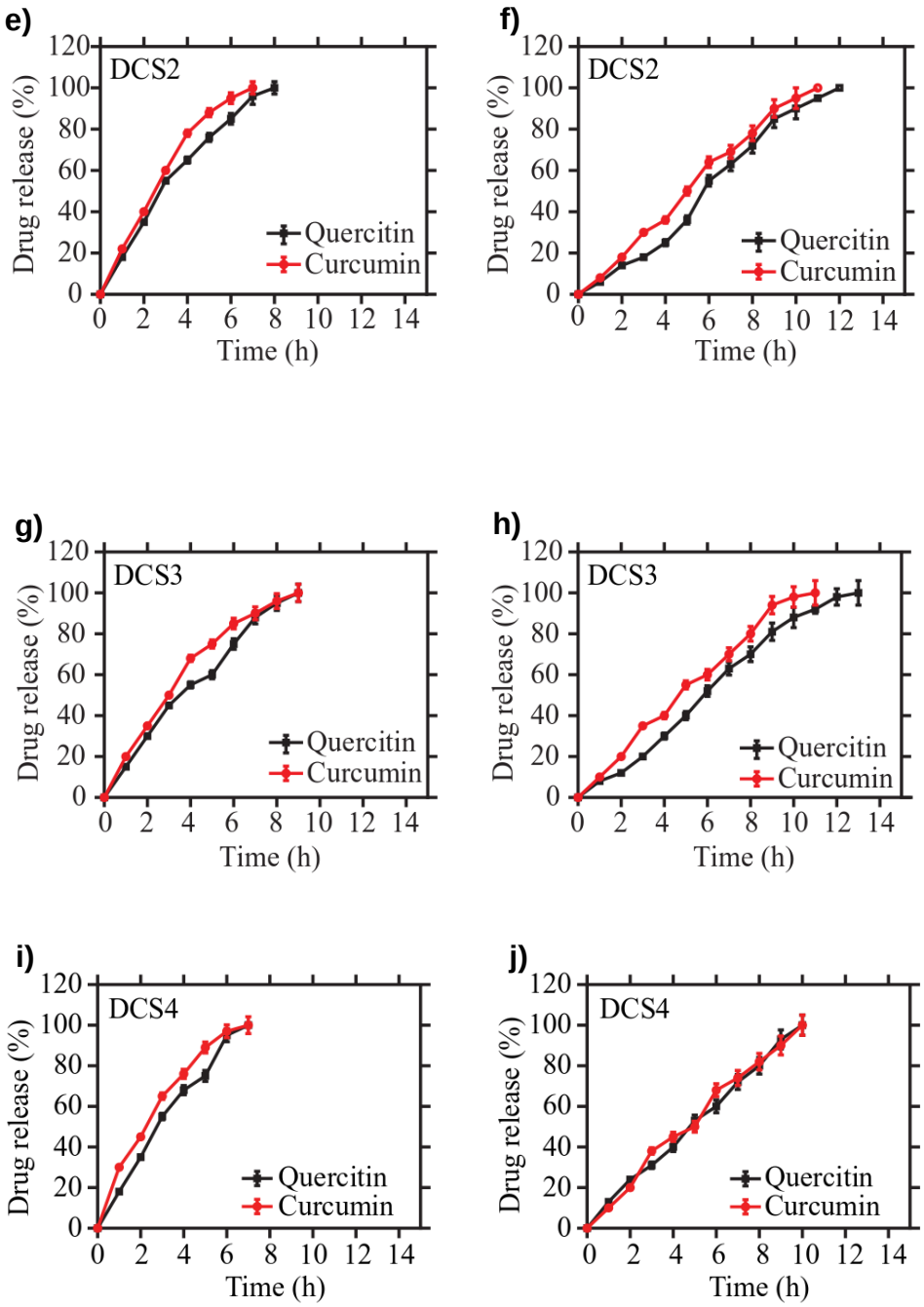

Figure 45. Cumulative percentage of Cur and QT released from **CS2** (a, b), **DCS1** (c, d), **DCS2** (e, f), **DCS3** (g, h) **DCS4** (I, j) at pH 5.5 (left column) and pH 7.4 (right column), respectively.

A crucial requirement for formulating poorly water-soluble drugs is the enhancement of their bioavailability via increasing the local concentration of the active ingredient in the vicinity of the target cell. This requires a controlled drug release from the microcarrier particles. In good agreement with this precondition, upon formulating the drug as a molecular dispersion adsorbed into the different compartments of the present silica microparticles, a rapid release from the **DCS3** and **DCS4** particles was observed. There are reports that it took 30 h to complete the release of the drug captopril and that it took 19 h for the complete release of 5-fluorouracil from their mesoporous silica particles.[145] Even though there are drug release studies on mesoporous silica particles, the time taken for releasing the loaded drug is typically much larger than the time period for 100 % drug release observed in the present study.

4.2.6 Cell viability assay

Typical for cancer cells is the uncontrolled proliferation of the cells. Thus, a treatment ideally causes cell death specifically to cancer cells. The non-toxicity of quercetin, curcumin and mesoporous silica particles on normal cells were reported elsewhere.[37,146,147] The cytotoxicity of Cur and QT loaded on **CS2**, **DCS3** and **DCS4** individually as well as in combination were examined by performing the 3-(4,5-dimethylthiazol-2-yl)-2,5-diphenyltetrazolium bromide (MTT) assay against human bone osteosarcoma epithelial cell lines (U2OS).[148] The results indicate that Cur and QT loaded particles had significant toxicity towards the U2OS cancer cells and that the activity strongly depended on the amounts of drugs loaded, the shape and the amphiphilic character of the silica particles (Figure 46, Table 11).

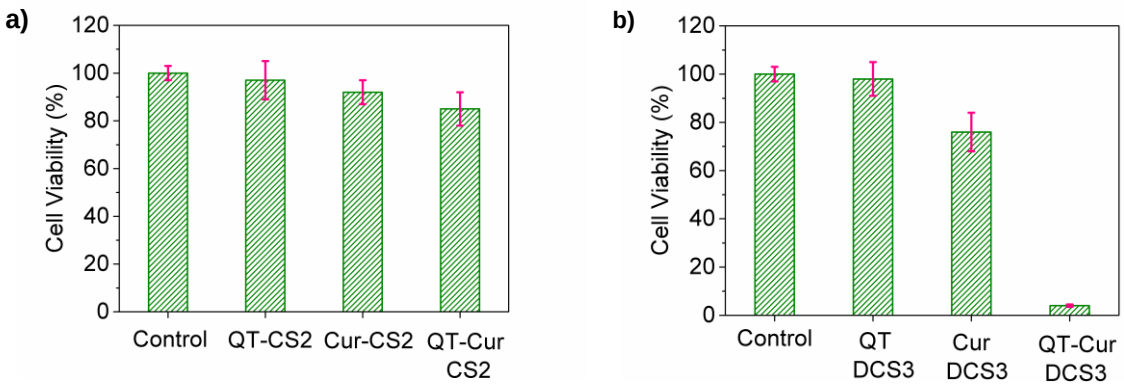

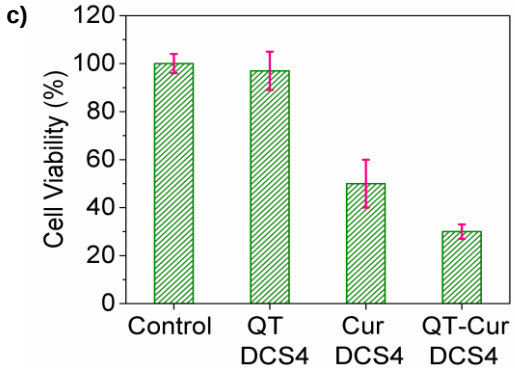

Figure 46: Cell viability assays after 24 h incubation of U2OS cancer cells with a) **CS2** alone, QT-**CS2**, Cur-**CS2** and QT-Cur-**CS2**; b) **DCS3** alone, QT-**DCS3**, Cur-**DCS3** and QT-Cur-**DCS3**; c) **DCS4** alone, QT-**DCS4**, Cur-**DCS4** and QT-Cur-**DCS4** at 25 nM. The data represent the average of at least three independent measurements.

The IC_{50} concentration of QT-**CS2**, Cur-**CS2** and Cur-QT-**CS2** were 200, 150 and 100 nM for the respective drug loaded **CS2** particles. Figure 42 displays the results of the cytotoxicity for QT loaded, Cur loaded and both drugs loaded silica particles **CS2**, **DCS3** and **DCS4**. The QT-**CS2**, Cur-**CS2** and Cur-QT-**CS2** particles showed 97 %, 95 % and 92 % cell viability, respectively, at 25 nM concentration after 24 h (Figure 46a). The respective epi-fluorescence and phase contrast images (Figure 47) for the QT-**CS2**, Cur-**CS2** and Cur-QT-**CS2** also show that the cells did not undergo any morphological changes or cell death after 24 h.

For the QT-**DCS4**, Cur-**DCS4** and Cur-QT-**DCS4** particles, about 97 %, 50 % and 30 % of cell viability was observed at 25 nM of drug concentration, respectively, as shown in the Figure 46c. The higher cell toxicity of Cur-**DCS4** compared to Cur-**CS2** is attributed to the higher concentration of Cur delivered by **DCS4** (Table 11).

The viability of the cells at 25 nM concentration for QT-**DCS3**, Cur-**DCS3** and Cur-QT-**DCS3** was around 85 %, 79 % and 4 % after 24 h (Figure 46b). In the same order, the IC_{50} was found to be 105, 57 and 13.5 nM, respectively, after 24 h. Note that the IC_{50} for Cur and QT alone is 21.6 and 100 µM, respectively.[149,150] Thus, the drug loaded **DCS3** particles showed an enhanced effect even at nanomolar concentrations when compared to drug loaded **CS** and drugs alone.

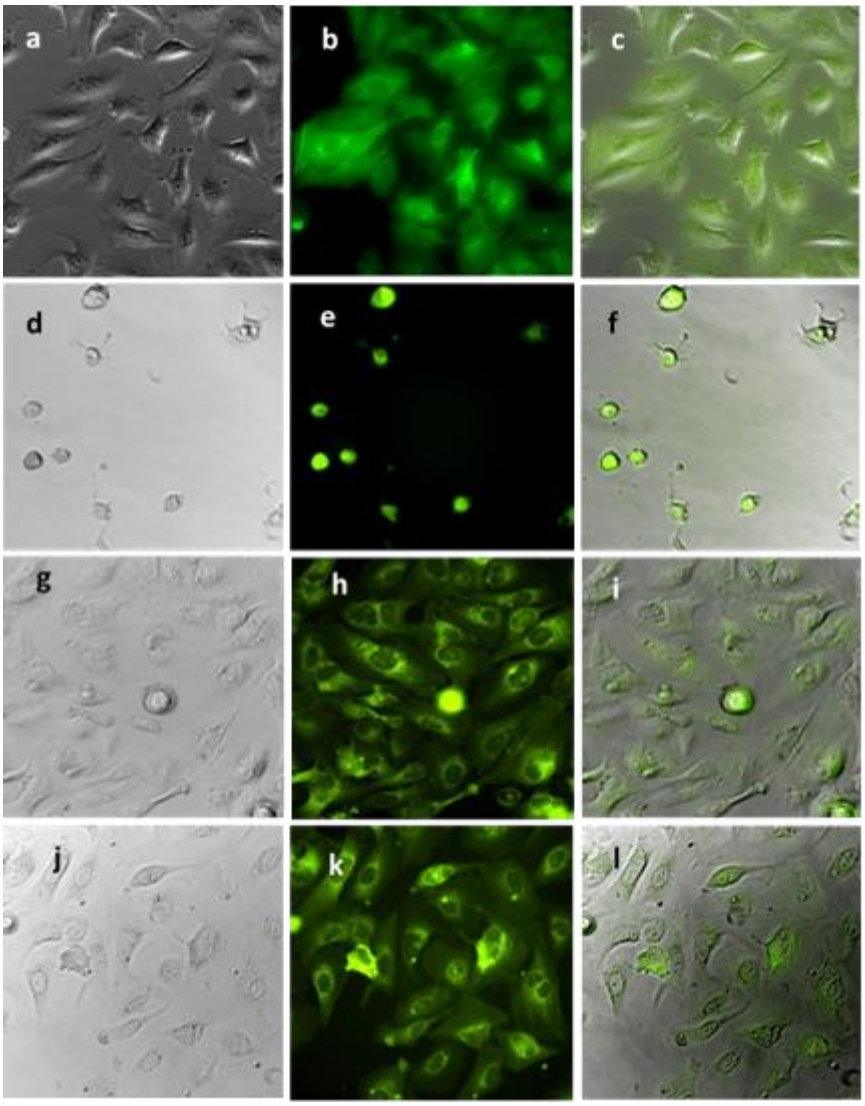

Figure 47: Phase contrast (first column), epifluorescence (second column) and overlaid (third column) images of tU2O cell lines. (a-c) U2OS cells treated with **CS2** alone; (d-f) Cells treated with Cur-QT-**CS2**; (g-i) Cells treated with Cur-**CS2**; (j-l) Cells treated with QT-**CS2** at 25 nM concentration for 24 h.

The corresponding cell images of **DCS3** after 24 h are shown in Figure 47. Figures 47a-c show the phase contrast, epi-fluorescence and overlay images of the cells, respectively, when treated with **DCS3** without drugs. All cells were viable and no cytotoxicity was observed from **DCS3**, which agrees with reports that silica particles are nontoxic to cells.[23] When cells were treated with drug loaded Cur-QT-**DCS3** at 25 nM, changes in the cell morphology were observed. The cells died either because of necrosis or apoptosis as shown in the Figures 48d-f. Figures 48g-i and 48j-l correspond to cells treated with Cur-**DCS3** and QT-**DCS3**, respectively, at 25 nM concentration. Also in this case changes in the morphological structure of the cells

were observed. Thus, one can conclude that the Cur-QT-**DCS3** particles had a greater cytotoxicity effect than the Cur-QT-**CS** and Cur-QT-**DCS4** particles.

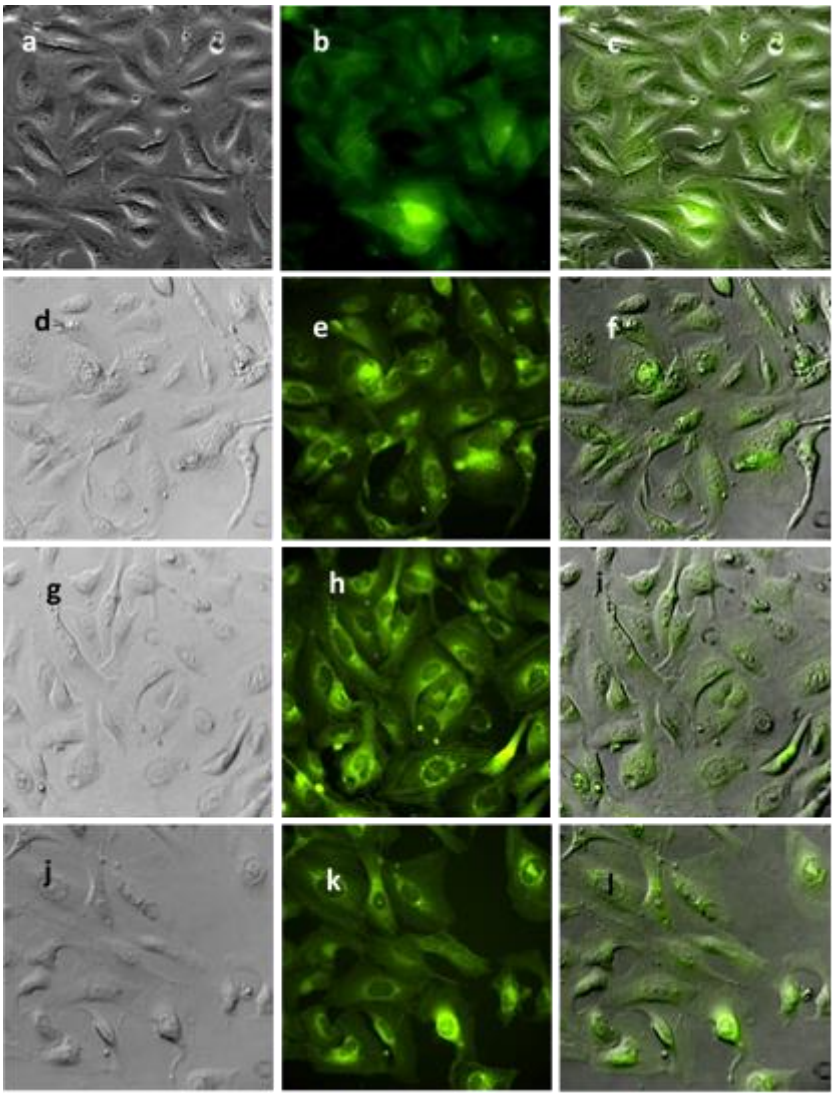

Figure 48: Phase contrast (first column), epifluorescence (second column) and overlaid (third column) images of the U2Os cell lines. (a-c) U2OS cells treated with **DCS3** alone; (d-f) Cells treated with Cur-QT-**DCS3**; (g-i) Cells treated with Cur-**DCS3**; (j-l) Cells treated with QT-**DCS3** at 25 nM concentration for 24h.

4.3 Conclusion

Varying the stirring speed and the added salts in a simple etching process of micron sized silica particles allowed the syntheses of spherical core-shell **CS1,2**, anisotropic core-shell **DCS4** and anisotropic and amphiphilic core-shell **DCS1-3** silica particles. The three types of particles show diverse architectures that provide mesoporous channels, hollow cavities and anisotropic surface charge distributions. The porous shells and the cavity allowed accumulating several molecules. The differential distribution was demonstrated by loading the polyphenols QT and Cur into the mesopores and cavities of the particles. The loading behavior of these two drugs varied significantly between the three particles. Moreover, the anisotropic and amphiphilic core-shell **DCS3** particle was able to discriminate between Cur and QT by accumulating them in different areas of the particle. Cell viability studies also showed major differences among the three drug-loaded particles. While the effect of drug loaded **CS2** on cells was moderate, the cell toxicity increased from drug loaded **DCS4** to drug loaded **DCS3**. Most interestingly, although **CS2** and **DCS3** delivered comparable amounts of both drugs, the cell toxicity of Cur-QT-**DCS3** was dramatically higher compared to Cur-QT-**CS2**. Apparently, the anisotropic character in shape and surface charge of **DCS3** allowed for a much better interaction of the drug loaded particle with the cells.[57] In the future, different pairs of drugs can be tested for other treatments.

Chapter 5. Experimental Part

5.1 Solvents, reagents and equipment

The following chemicals were used without further purification: For all reactions HPLC grade water was used. Ammonium hydroxide (NH_4OH) (28-30 %) was purchased from Sigma Aldrich. Ammonium fluoride (NH_4F) (96%), silica particles (1.5 µm and 1.0 µm, 99.9%), tetraethoxysilane (TEOS, 99%), phenyltrimethoxysilane (PTMS, 97%), mercaptotrimethoxysilane (MerTMS, 95%), polyvinyl alcohol and *n*-tridecane (98%) were obtained from ABCR. Toluene, n-hexane and mesitylene were bought from Fischer Chemical. Rhodamine 6g, sulforhodamine B, atto amine 488, Alexa 514, curcumin and quercetin were purchased from Sigma Aldrich.

5.2 General protocol of T group particles

To a stirring solution of 115 mL of water and 0.266 mL of aqueous NH_4OH (28–30 %) 2.58 mL is added a mixture of the corresponding T-group silane and optionally TEOS and /or an organic solvent (Tables 13-16.) over a period of 40 minutes with a syringe pump. After the mixture has been added completely the solution was stirred at room temperature for 16 hours. After the solvent has been removed, the particles were washed with water, ethanol and dried in the oven at 70 °C for 16 hours.

5.3 General protocol of dumbbell particles

The anisotropic dumbbell core-shell silica particles were synthesized by following a procedure reported earlier[111] with minor variations. Concisely, 2.1 g CTAB as surfactant, 2.1 g silica particles of 1.5 µm size were dissolved in 210 mL of water and sonicated for an hour. Then 11.6 mL *n*-tridecane was added and sonicated for another hour. To this suspension 12 mL of an ammonia and ammonium fluoride (1.35 mmol) solution was added and kept stirring at 210-240 rpm at 90 ^{o} C for 24 h. Particles were collected after centrifugation (2500 rpm for 1 min) and washed once with deionised water, twice with ethanol, once with diethyl ether and then calcined at 600 ^{o} C for 15 h.

5.4 Analytics

5.4.1 SEM (Scanning electron microscopy), STEM (Scanning transmission electron microscopy)

Scanning electron microscopy (SEM) and scanning transmission microscopy (STEM) images were acquired on a Hitachi SU8030 machine equipped with a triple detector. The particles were suspended in ethanol and kept in an ultrasonic bath for homogenization for 10 minutes. The samples were spin-coated onto silicon wafers for SEM and spotted on copper grids for STEM analysis. The particle diameters were determined by measuring 100 particles Figure 49 by hand using Image J. In the case of the bowl like particles, the long distance was used to determine the size.

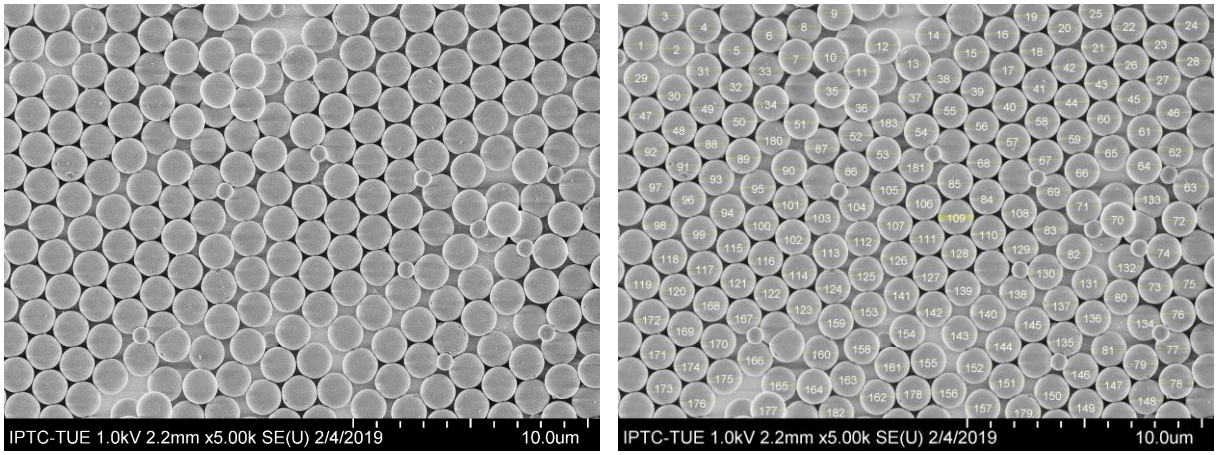

a) original Image **b) evaluated Image**

Figure 49: Illustration of the evaluation of particle sizes from a SEM image.

Table 12: Calculation of d10, d50 and d90 with Qtiplot

Size	Description	Calculation
d^{10}	10% of all particles are smaller than this value	Manual (Data, 0.1)
d^{50}	10% of all particles are smaller than this value	Median (Data)
d^{90}	10% of all particles are smaller than this value	Manual (Data, 0.9)

5.4.2 Zeta potential, dynamic light scattering (DLS)

The zeta potential in water and DLS in ethanol were measured at room temperature with a Zetasizer Nano ZS by Malvern. The samples were suspended in distilled water and transferred to a cuvette. Suspension in the measuring cell was almost clear. The concentration compared optically with a well measured sample

5.4.3 Confocal microscope

Confocal light microscopy was performed by Leica TCS SP8 Multiphoton Confocal Microscope. 2 mg of the sample were suspended in ethanol with a 1:1 mixture of the corresponding dye and 4% of PVA. The solution was placed onto a glass substrate to obtain individual particles on the substrate. The PVA is used to keep the particles fixed during measurement. The concentrations of the respective dye was varied to obtain a satisfactory result.

5.4.4 Physisorption

N_2-physisorption measurements were performed on an ASAP2020 volumetric adsorption apparatus (Micromeritics Instrument Corp.) at 77 K (a_m (N_2, 77 K) = 0.162 nm^2). The samples were degassed at 250 °C for 4 h prior to analysis. The Brunauer–Emmett–Teller (BET) specific surface area was calculated from the nitrogen adsorption branch of the isotherm in the relative pressure range of 0.07–0.15 for the pure SiO_2 materials and the hybrid materials. Pore size distributions (dV/dD) were calculated from the nitrogen desorption branch using the Barrett–Joyner–Halenda (BJH) method.

5.4.5 Nuclear magnetic resonance (NMR) spectroscopy:

^{13}C and ^{29}Si solid state NMR spectra were recorded using the CP/MAS and HPDEC technique on an AVIIIHD-300WB NMR spectrometer from Bruker.

5.4.6 Diffuse reflectance infra-red Fourier Transform (DRIFT) spectroscopy

Drift spectra were collect with the Vertex 70 FT-IR spectrometer from Bruker. A finely grained KBr was used for the background measurement 0.5 mg of the sample were mixed with 25 mg KBr and then finely grained to collect spectra.

5.4.7 Raman spectroscopy

For Raman measurements, a WITec alpha300 RA&S confocal Raman microscope was used. This system is equipped with a lens-based UHTS 300 spectrometer connected via a 100 µm (NA=0.12) multi-mode optical fibre and thermoelectric cooled CCD and EMCCD (DU970N-BV). All Raman experiments were carried out using a laser of 532 nm with a nominal output power of 60 mW and a grating of 600 lines/mm. For illumination and collection the laser was focused on the sample through a Zeiss Epiplan-Neofluar objective of magnification 100x (NA = 0.9). Data procession was done using Control 5.0 software provided by WITec and all experiments were carried out at ambient conditions. We chose sapphire as a substrate due to its low background signal which does not overshadow the signal intensity from the region of interest. The peak positions of sapphire also do not interfere with the potential peak positions of QT and Cur, thus making sapphire an ideal substrate for Raman analysis of these drug loaded particles. The samples were prepared in the same way as described in the drug loading experiments.

5.5 Drug loading of curcumin (Cur) and quercetin (QT)

For loading the microparticles with drugs, 0.5 mg/mL of an equimolar solution of Cur and QT, respectively, in ethanol was mixed with 1 mg/mL of the corresponding microparticles. The suspensions were shortly ultrasonicated and gently stirred for 4 h. Then, the Cur and QT loaded microparticles were centrifuged at 13,000 rpm for 3 min. The drug loading efficiency was detected by measuring UV-absorbance (Nanodrop, ND 1000 spectrometer) of Cur and QT at 450 and 270 nm, respectively, in the supernatants of the centrifuged sample and the initial 0.5 mg/mL solution. The following equation was used to determine the drug loading content of both drugs in the microparticles.

$$\text{Drug loading efficiency} = \frac{\text{Theoretical amount of drug loaded - Free drug}}{\text{Theoretical amount of drug loaded}} \times 100$$

5.6 In vitro drug release study

In vitro drug release studies of Cur and QT were investigated at pH 5.5 (environmental pH for tumors) and at pH 7.4 (physiological pH). The drug loaded particles were suspended in 2 mL of phosphate-buffered saline (PBS) and transferred to a dialysis bag (molecular weight cut-off 10 kDa, Sigma). Then they were placed in 25 mL of PBS, incubated at 37 °C and kept under stirring (100 rpm).[151,152] The released drugs were determined spectrophotometrically by

measuring the absorbance at 450 and 270 nm. The concentration of released drug was then calculated using the standard curve of drugs as mentioned.[151,152] The percentage of drug released was determined from the following equation as described earlier.[153,154]

$$\text{Cumulative drug release (\%)} = \frac{\text{Cumulative amount released}}{\text{Total mass loaded}} \times 100$$

5.7 Cell viability studies

The cytotoxicity of the cells was studied by performing the 3-(4,5-dimethylthiazol-2-yl)-2,5-diphenyltetrazoliumbromide (MTT) assay as described.[148] Briefly, the human bone osteosarcoma epithelial cancer cell lines (U2OS; 6x103 cells) were seeded in a 96 well culture plate. After 12 h, the cells were treated with different concentrations of the drug loaded particles for 24 h. Control cells were treated with 0.1% DMSO in a culture medium. After treatment, the cells were incubated with the MTT solution (5 mg/mL in PBS) at 37°C for 4 h and then DMSO was added during shaking at room temperature. The spectrophotometric absorbance was measured at 570 nm on a microplate reader (Biotek, Multiplate reader, USA). Cell viability was expressed as the relative formazan formation in the treated samples compared with control cells after correction for background absorbance. The cytotoxicity (IC50) was calculated based on the colour yield of the treated cells which are proportional to the number of metabolically active cells and indirectly approximated cell viability. IC50 is defined as the drug concentration required to inhibit growth of cells by 50 % relative to control (IC50). A graph was drawn using Cell viability (%) with respect to the concentration of the sample. Results were plotted as the mean ± SD of three separate experiments. Percentage of cell viability was determined using the below formula.[148]

$$\text{Cell Viability (\%)} = \frac{\text{Absorbance of the treated sample}}{\text{Absorbance of the untreated sample}} \times 100$$

5.8 Experimental Tables:

Table 13 VTMS				
	TEOS : VTMS [mL]	Reaction time	Particle size [µm]	comment
V1	4.96 : 14.28	50 min	4.6	
V2	"	80 min	2.9	
V3	"	15 h	2.7	
V4	"	17 h	2.9	
V5	"	19 h	3.4	
V6	"	24 h	3.6	Drop rate 58ml/h
V7	4.96 : 6.8	50 min	1.9	
V8	4.96 : 3.4	50 min	2.7	
V9	19.8 : 3.4	50 min	1.7	

Table 14 PTMS				
	TEOS : PTMS [molar ratio]	Organic solvent [mmol]	Particle size [µm]	Comment
P1	22 : 88 mmol	--	4	plane
P1a	22 : 44	--		
P1b	22 : 22	--		
P1c	44 : 22.3	--		
P1d	42.7 : 22.1	--	1.9	
P2	44.2 : 22	--	4.5	RT long
P3	22 : 88	3.29 mmol, Hexane	3.8	
P4	-	5.35 (2 h later)	2.3	
P5	-	5.35	2.1	
P6		6.58	1.7	
P7	-	3.29 mmol, Toluene	2.3	
P8		5.54	2.4	
P9	-	5.63	1.3	
P10	-	6.57	1.5	
P11	-	3.31 mmol, Mesitylene	2.7	
P12	-	5.61	2.8	
P13	-	8.99	2.5	
P14	-	8.77	2.4	600 rpm
P15		"	1.9	300 rpm
P16	-	"	2.1	600 rpm
P17	-	"	2.4	200 rpm 18ml/h
P18	-	"	3.2	600 rpm 72ml/h

(-) represents same amount and (--) represents no addition of solvents.

Table 15 MerTMS

	TEOS : MerTMS [mL/mmol]	Organic solvent [mL/mmol]	Comment	Particle size [µm]
M 1	22 mmol : 88.3 mmol		17 h	3.8
M 2	"		14 h	2.9
M 3	"		10 h	2.4
M 4	0 : 88.3 mmol (No TEOS)	5.61 mmol, Mesitylene	Short RT	
M 5	54.9 mmol	"		1.7
M 6	88.3 mmol	"		3.7
M 7	110 mmol	"		3.5
M 8	88.3 mmol	"	Long RT	
M 9	110 mmol	2.29 mmol Hexane		4.4
M 10	"	3.06		3.8
M 11	"	4.59		2.7
M 12	"	18.4		2.9
M 13	"	41.8, n-tridecane		2.5
M 14	"	10.8 (Mechanical stirrer)		1.9
M15	"	5.26	5	1.
M16	"	8.04	4.7	1.2
M17	"	9.64		1.4
M18	"	10		1.5
M19	"	10.8		1.6
M20	"	11.3		1.7

M21	"	11.7	1.7
M22	"	12.1	1.7
M 23	"	10 (8h)	1.52
M 24	"	10.8 (8h)	1.57
M 25	"	12.1 (8h)	1.40
M 26	"	10 (16 hrs)	1.57
M 27	"	10.8 (16 hrs)	1.75
M 28	"	12.1 (16 hrs)	1.93

(") represents same amount and (--) represents no addition of solve

Chapter 6. References

(1) Ma, J. F. *Crit. Rev. Plant Sci.* **2005**, *24* (4), 267–281.

(2) Wang, H.; Yu, M.; Lin, C. K.; Lin, J. *J. Colloid Interface Sci.* **2006**, *300* (1), 176–182.

(3) Suratwala, T.; Steele, R.; Feit, M. D.; Wong, L.; Miller, P.; Menapace, J.; Davis, P. *J. Non-Cryst. Solids* **2008**, *354* (18), 2023–2037.

(4) Janzen, R.; Unger, K. K.; Giesche, H.; Kinkel, J. N. IV.

(5) Walther, A.; Müller, A. H. E. *Chem. Rev.* **2013**, *113* (7), 5194–5261.

(6) Singh, L. P.; Bhattacharyya, S. K.; Kumar, R.; Mishra, G.; Sharma, U.; Singh, G.; Ahalawat, S. *Adv. Colloid Interface Sci.* **2014**, *214*, 17–37.

(7) Keshavarz, M.; Ahmad, N. *J. Nanoparticles* **2013**, *2013*, 1–4.

(8) Fang, X.; Chen, C.; Liu, Z.; Liu, P.; Zheng, N. A *Nanoscale* **2011**, *3* (4), 1632–1639.

(9) Ditzinger, F.; Price, D. J.; Ilie, A.-R.; Köhl, N. J.; Jankovic, S.; Tsakiridou, G.; Aleandri, S.; Kalantzi, L.; Holm, R.; Nair, A.; Saal, C.; Griffin, B.; Kuentz, M. *J. Pharm. Pharmacol.* **2019**, *71* (4), 464–482.

(10) Barbé, C.; Bartlett, J.; Kong, L.; Finnie, K.; Lin, H. Q.; Larkin, M.; Calleja, S.; Bush, A.; Calleja, G. *Adv. Mater.* **2004**, *16* (21), 1959–1966.

(11) Biswas, A.; Shukla, A.; Maiti, P. *Langmuir* 2019, 35,38, 12285-12305.

(12) Hoffman, A. S. *J. Controlled Release* **2008**, *132* (3), 153–163.

(13) Folkman, J. *Biomaterials* **1990**, *11* (9), 615–618.

(14) Park, K. *J. Control. Release Soc.* **2014**, *190*, 3–8.

(15) Allen, T. M.; Cullis, P. R. *Adv. Drug Deliv. Rev.* **2013**, *65* (1), 36–48.

(16) Böhme, D.; Beck-Sickinger, A. G. *J. Pept. Sci. Off. Publ. Eur. Pept. Soc.* **2015**, *21* (3), 186–200.

(17) Logie, J.; Owen, S. C.; McLaughlin, C. K.; Shoichet, M. S. *Chem. Mater.* **2014**, *26* (9), 2847–2855.

(18) Skorb, E. V.; Möhwald, H. "Smart" Surface Capsules for Delivery Devices. *Adv. Mater. Interfaces* **2014**, *1* (6), 1400237.

(19) Gong, M.-Q.; Wu, J.-L.; Chen, B.; Zhuo, R.-X.; Cheng, S.-X. *Langmuir* **2015**, *31* (18), 5115–5122.

(20) Morales, V.; Idso, M. N.; Balabasquer, M.; Chmelka, B.; García-Muñoz, R. A. *J. Phys. Chem. C* **2016**, *120* (30), 16887–16898.

(21) Geng, H.; Zhao, Y.; Liu, J.; Cui, Y.; Wang, Y.; Zhao, Q.; Wang, S. *Int. J. Pharm.* **2016**, *510* (1), 184–194.

(22) Lainé, A.-L.; Price, D.; Davis, J.; Roberts, D.; Hudson, R.; Back, K.; Bungay, P.; Flanagan, N. *Int. J. Pharm.* **2016**, *512* (1), 118–125.

(23) Tarn, D.; Ashley, C. E.; Xue, M.; Carnes, E. C.; Zink, J. I.; Brinker, C. J. *Acc. Chem. Res.* **2013**, *46* (3), 792–801.

(24) Joshi, R.; Feldmann, V.; Koestner, W.; Detje, C.; Gottschalk, S.; Mayer, H. A.; Sauer, M. G.; Engelmann, J. *Biol. Chem.* **2013**, *394* (1), 125–135.

(25) Heikkilä, T.; Salonen, J.; Tuura, J.; Kumar, N.; Salmi, T.; Murzin, D. Y.; Hamdy, M. S.; Mul, G.; Laitinen, L.; Kaukonen, A. M.; Hirvonen, J.; Lehto, V.-P. *Drug Deliv.* **2007**, *14* (6), 337–347.

(26) Yang, Y.-Y.; Wang, X.; Hu, Y.; Hu, H.; Wu, D.-C.; Xu, F.-J. *ACS Appl. Mater. Interfaces* **2014**, *6* (2), 1044–1052.

(27) Yang, Y.; Achazi, K.; Jia, Y.; Wei, Q.; Haag, R.; Li, J. *Langmuir ACS J. Surf. Colloids* **2016**, *32* (47), 12453–12460.

(28) Kresge, C. T.; Leonowicz, M. E.; Roth, W. J.; Vartuli, J. C.; Beck, J. S. *Nature* **1992**, *359* (6397), 710–712.

(29) Brinker, C. J.; Lu, Y.; Sellinger, A.; Fan, H. *Adv. Mater.* **1999**, *11* (7), 579–585.

(30) Zhao, D.; Huo, Q.; Feng, J.; Chmelka, B. F.; Stucky, G. D. *J. Am. Chem. Soc.* **1998**, *120* (24), 6024–6036.

(31) Wan, Y.; Zhao, D. *Chem. Rev.* **2007**, *107* (7), 2821–2860.

(32) Galarneau, A.; Iapichella, J.; Bonhomme, K.; Di Renzo, F.; Kooyman, P.; Terasaki, O.; Fajula, F. *Adv. Funct. Mater.* **2006**, *16* (13), 1657–1667.

(33) Huh, S.; Wiench, J. W.; Trewyn, B. G.; Song, S.; Pruski, M.; Lin, V. S. Y. *Chem. Commun. Camb. Engl.* **2003**, No. 18, 2364–2365..

(34) Travaglini, L.; De Cola, L. *Chem. Mater.* **2018**, *30* (12), 4168–4175.

(35) Luo, L.; Liang, Y.; Chassé, T.; Anwander, R. *Part. Part. Syst. Charact.* **2018**, *35* (12), 1800312.

(36) Torney, F.; Trewyn, B. G.; Lin, V. S.-Y.; Wang, K. *Nat. Nanotechnol.* **2007**, *2* (5), 295–300.

(37) Slowing, I. I.; Vivero-Escoto, J. L.; Wu, C.-W.; Lin, V. S.-Y. *Adv. Drug Deliv. Rev.* **2008**, *60* (11), 1278–1288.

(38) Zha, J.; Roggendorf, H. Ed. by C. J. Brinker and G. W. Scherer, Academic Press, Boston 1990, Xiv, 908 Pp., Bound—ISBN 0-12-134970-5. *Adv. Mater.* **1991**, *3* (10), 522–522.

(39) Hench, L. L.; West, J. K. *Chem. Rev.* **1990**, *90* (1), 33–72.

(40) Costa, C. A. R.; Leite, C. A. P.; Galembeck, F. *J. Phys. Chem. B* **2003**, *107* (20), 4747–4755.

(41) Plumeré, N.; Ruff, A.; Speiser, B.; Feldmann, V.; Mayer, H. A. *J. Colloid Interface Sci.* **2012**, *368* (1), 208–219.

(42) Wright, J. D.; Sommerdijk, N. A. J. M.; Sommerdijk, N. A. J. M. *Sol-Gel Materials : Chemistry and Applications*; CRC Press, 2018.

(43) Stöber, W.; Fink, A.; Bohn, E. **1968**, *26* (1), 62–69.

(44) Stöber, W.; Fink, A.; Bohn, E. *J. Colloid Interface Sci.* **1968**, *26* (1), 62–69.

(45) Wang, X.-D.; Shen, Z.-X.; Sang, T.; Cheng, X.-B.; Li, M.-F.; Chen, L.-Y.; Wang, Z.-S. *J. Colloid Interface Sci.* **2010**, *341* (1), 23–29.

(46) Arantes, T. M.; Pinto, A. H.; Leite, E. R.; Longo, E.; Camargo, E. R. *Colloids Surf. Physicochem. Eng. Asp.* **2012**, *415*, 209–217.

(47) Beygi, H.; Karimi, E. Z.; Farazi, R.; Ebrahimi, F. *J. Alloys Compd.* **2016**, *654*, 308–314.

(48) Qi, D.; Lin, C.; Zhao, H.; Liu, H.; Lü, T. *J. Dispers. Sci. Technol.* **2017**, *38* (1), 70–74.

(49) Luo, X.; Dong, J.; Zhang, L.; Du, J.; Wang, H.; Gao, W. *J. Sol-Gel Sci. Technol.* **2017**, *81* (3), 669–677.

(50) Tan, C. G.; Bowen, B. D.; Epstein, N. *J. Colloid Interface Sci.* **1987**, *118* (1), 290–293.

(51) Bogush, G. H.; Zukoski, C. F. *J. Colloid Interface Sci.* **1991**, *142* (1), 19–34.

(52) LaMer, V. K.; Dinegar, R. H. *J. Am. Chem. Soc.* **1950**, *72* (11), 4847–4854.

(53) Blaaderen, A. V.; Geest, J. V.; Vrij, A. *J Col Inter Sci* **1992**.

(54) Bogush, G. H.; Zukoski, C. F. *J. Colloid Interface Sci.* **1991**, *142* (1), 1–18.

(55) Park, S. K.; Kim, K. D.; Kim, H. T. *Colloids Surf. Physicochem. Eng. Asp.* **2002**, *197* (1), 7–17.

(56) Meyer, F.; Hempelmann, R.; Mathur, S.; Veith, M. *J. Mater. Chem.* **1999**, *9* (8), 1755–1763.

(57) Li, T.; Moon, J.; Morrone, A. A.; Mecholsky, J. J.; Talham, D. R.; Adair, J. H. *Langmuir* **1999**, *15* (13), 4328–4334.

(58) Mokari, T.; Sertchook, H.; Aharoni, A.; Ebenstein, Y.; Avnir, D.; Banin, U. *Chem. Mater.* **2005**, *17* (2), 258–263.

(59) Santra, S.; Tapec, R.; Theodoropoulou, N.; Dobson, J.; Hebard, A.; Tan, W. *Langmuir* **2001**, *17* (10), 2900–2906.

(60) Darbandi, M.; Thomann, R.; Nann, T. *Chem. Mater.* **2005**, *17* (23), 5720–5725.

(61) Gupta, A. K.; Gupta, M. *Biomaterials* **2005**, *26* (18), 3995–4021.

(62) Lindner, null; Schneller, null; Auer, null; Mayer, null. *Angew. Chem. Int. Ed Engl.* **1999**, *38* (15), 2154–2174.

(63) Ghosh Chaudhuri, R.; Paria, S. *Chem. Rev.* **2012**, *112* (4), 2373–2433.

(64) Caruso, F. *Adv. Mater.* **2001**, *13* (1), 11–22.

(65) Burns, A.; Ow, H.; Wiesner, U. *Chem. Soc. Rev.* **2006**, *35* (11), 1028–1042.

(66) Salgueiriño-Maceira, V.; Spasova, M.; Farle, M. *Adv. Funct. Mater.* **2005**, *15* (6), 1036–1040.

(67) Choi, H.; Chen, I.-W. *J. Colloid Interface Sci.* **2003**, *258* (2), 435–437.

(68) Hayes, R.; Ahmed, A.; Edge, T.; Zhang, H. *J. Chromatogr. A* **2014**, *1357*, 36–52.

(69) Geiser, M.; Quaile, O.; Wenk, A.; Wigge, C.; Eigeldinger-Berthou, S.; Hirn, S.; Schäffler, M.; Schleh, C.; Möller, W.; Mall, M. A.; Kreyling, W. G. *Part. Fibre Toxicol.* **2013**, *10* (1), 19.

(70) Perro, A.; Reculusa, S.; Ravaine, S.; Bourgeat-Lami, E.; Duguet, E. *J. Mater. Chem.* **2005**, *15* (35–36), 3745.

(71) Müller, N.; Heinrich, C.; Abersfelder, K.; Kickelbick, G. *Chem. Unserer Zeit* **2016**, *50* (6), 392–399.

(72) Du, J.; O'Reilly, R. K. *Chem. Soc. Rev.* **2011**, *40* (5), 2402-2416

(73) Kaewsaneha, C.; Tangboriboonrat, P.; Polpanich, D.; Eissa, M.; Elaissari, A. *ACS Appl. Mater. Interfaces* **2013**, *5* (6), 1857–1869.

(74) Monson, P. A. *Microporous Mesoporous Mater.* **2012**, *160*, 47–66.

(75) Beck, J. S.; Vartuli, J. C.; Roth, W. J.; Leonowicz, M. E.; Kresge, C. T.; Schmitt, K. D.; Chu, C. T. W.; Olson, D. H.; Sheppard, E. W.; McCullen, S. B.; Higgins, J. B.; Schlenker, J. L. *J. Am. Chem. Soc.* **1992**, *114* (27), 10834–10843.

(76) Wilke, T.; Haffer, S.; Tiemann, M.; Waitz, T. *CHEMKON* **2012**, *19* (2), 67–72.

(77) Voort, P. V. D.; Vercaemst, C.; Schaubroeck, D.; Verpoort, F. *Phys. Chem. Chem. Phys.* **2008**, *10* (3), 347–360.

(78) Tanev, P. T.; Pinnavaia, T. J. *Science* **1995**, *267* (5199), 865–867.

(79) Kao, H.-M.; Ting, C.-C.; Chiang, A. S. T.; Teng, C.-C.; Chen, C.-H. *Chem. Commun.* **2005**, No. 8, 1058.

(80) Katiyar, A.; Yadav, S.; Smirniotis, P. G.; Pinto, N. G. *J. Chromatogr. A* **2006**, *1122* (1–2), 13–20.

(81) Croissant, J. G.; Cattoën, X.; Durand, J.-O.; Wong Chi Man, M.; Khashab, N. M. *Nanoscale* **2016**, *8* (48), 19945–19972.

(82) Yin, J.; Deng, T.; Zhang, G. *Appl. Surf. Sci.* **2012**, *258* (6), 1910–1914.

(83) Knopp, D.; Tang, D.; Niessner, R. *Anal. Chim. Acta* **2009**, *647* (1), 14–30.

(84) Jung, C. Y.; Kim, J. S.; Kim, H. Y.; Ha, J. M.; Kim, Y. H.; Koo, S. M. *J. Colloid Interface Sci.* **2012**, *367* (1), 67–73.

(85) Palza, H.; Delgado, K.; Curotto, N. *Appl. Surf. Sci.* **2015**, *357*, 86–90.

(86) Zhou, Q.; Xiang, H.; Fan, H.; Yang, X.; Zhao, N.; Xu, J. *J. Mater. Chem.* **2011**, *21* (34), 13056–13061.

(87) Wang, Q.; Liu, Y.; Yan, H. *Chem. Commun.* **2007**, No. 23, 2339–2341.

(88) Lee, Y.-G.; Park, J.-H.; Oh, C.; Oh, S.-G.; Kim, Y. C. *Langmuir* **2007**, *23* (22), 10875–10878.

(89) Oh, C.; Shim, S.-B.; Lee, Y.-G.; Oh, S.-G. *Mater. Res. Bull.* **2011**, *46* (11), 2064–2069.

(90) Kadowaki, K.; Ishii, H.; Nagao, D.; Konno, M. *Langmuir* **2016**, *32* (44), 11600–11605.

(91) Abu-Zied, B. M.; Hussein, M. A.; Asiri, A. M. *Compos. Part B Eng.* **2014**, *58*, 185–192.

(92) Liu, H.; Ye, S.; Chen, Y. *China Particuology* **2005**, *3* (6), 379–382.

(93) Noda, I.; Kamoto, T.; Sasaki, Y.; Yamada, M. *Chem. Mater.* **1999**, *11* (12), 3693–3701.

(94) Deng, T.-S.; Zhang, Q.-F.; Zhang, J.-Y.; Shen, X.; Zhu, K.-T.; Wu, J.-L. *J. Colloid Interface Sci.* **2009**, *329* (2), 292–299.

(95) Li, X.; He, J. *ACS Appl. Mater. Interfaces* **2012**, *4* (4), 2204–2211.

(96) Yang, H.; Lu, X.; Xin, Z. *Langmuir* **2018**, *34* (39), 11723–11728.

(97) Meester, V.; Kraft, D. J. *Langmuir* **2016**, *32* (41), 10668–10677.

(98) Hao, N.; Nie, Y.; Zhang, J. X. J. *Microporous Mesoporous Mater.* **2018**, *261*, 144–149.

(99) Lo, C.-H.; Hu, T.-M. *Soft Matter* **2017**, *13* (35), 5950–5960.

(100) Hah, H. J.; Kim, J. S.; Jeon, B. J.; Koo, S. M.; Lee, Y. E. *Chem. Commun.* **2003**, No. 14, 1712–1713.

(101) Dong, H.; Brennan, J. D. *J. Mater. Chem.* **2012**, *22* (26), 13197.

(102) Thommes, M.; Kaneko, K.; Neimark, A. V.; Olivier, J. P.; Rodriguez-Reinoso, F.; Rouquerol, J.; Sing, K. S. W. *Pure Appl. Chem.* **2015**, *87* (9–10), 1051–1069.

(103) Motahari, A.; Hu, N.; Vahid, A.; Omrani, A.; Rostami, A. A.; Schaefer, D. W. *Langmuir ACS J. Surf. Colloids* **2018**, *34* (23), 6719–6726.

(104) Zhang, A.; Gu, L.; Hou, K.; Dai, C.; Song, C.; Guo, X. *RSC Adv.* **2015**, *5* (72), 58355–58362.

(105) Möller, K.; Bein, T. *Chem. Mater.* **2017**, *29* (1), 371–388.

(106) Cauda, V.; Schlossbauer, A.; Kecht, J.; Zürner, A.; Bein, T. *J. Am. Chem. Soc.* **2009**, *131* (32), 11361–11370.

(107) Tran, L.-T.-C.; Lesieur, S.; Faivre, V. *Expert Opin. Drug Deliv.* **2014**, *11* (7), 1061–1074.

(108) Luo, L.; Liang, Y.; Erichsen, E. S.; Anwander, R. Chemistry – A European Journal. May 17, 2018.

(109) Tuncelli, G.; Ay, A. N.; Zümreoglu-Karan, B. *Mater. Sci. Eng. C Mater. Biol. Appl.* **2015**, *55*, 562–568.

(110) Agrawal, G.; Agrawal, R. *ACS Appl. Nano Mater.* **2019**, *2* (4), 1738–1757.

(111) Maisch, J.; Jafarli, F.; Chassé, T.; Blendinger, F.; Konrad, A.; Metzger, M.; Meixner, A. J.; Brecht, M.; Dähne, L.; Mayer, H. A. *Chem. Commun.* **2016**, *52* (100), 14392–14395.

(112) Perro, A.; Reculusa, S.; Pereira, F.; Delville, M.-H.; Mingotaud, C.; Duguet, E.; Bourgeat-Lami, E.; Ravaine, S. *Chem. Commun. Camb. Engl.* **2005**, No. 44, 5542–5543.

(113) Deodhar, G. V.; Adams, M. L.; Trewyn, B. G. *Biotechnol. J.* **2017**, *12* (1), 1600408.

(114) Yu, M.; Gu, Z.; Ottewell, T.; Yu, C. Silica-Based Nanoparticles for Therapeutic Protein Delivery. *J. Mater. Chem. B* **2017**, *5* (18), 3241–3252.

(115) Dai, L.; Li, J.; Zhang, B.; Liu, J.; Luo, Z.; Cai, K. *Langmuir ACS J. Surf. Colloids* **2014**, *30* (26), 7867–7877.

(116) Li, R.; Xie, Y. *J. Control. Release Off. J. Control. Release Soc.* **2017**, *251*, 49–67.

(117) Zhao, Y.; Trewyn, B. G.; Slowing, I. I.; Lin, V. S.-Y. *J. Am. Chem. Soc.* **2009**, *131* (24), 8398–8400.

(118) Hewlings, S. J.; Kalman, D. S. *Foods Basel Switz.* **2017**, *6* (10).

(119) Nelson, K. M.; Dahlin, J. L.; Bisson, J.; Graham, J.; Pauli, G. F.; Walters, M. A. *J. Med. Chem.* **2017**, *60* (5), 1620–1637.

(120) Stanić, Z. *Plant Foods Hum. Nutr. Dordr. Neth.* **2017**, *72* (1), 1–12.

(121) Pallauf, K.; Rimbach, G. Autophagy, *Ageing Res. Rev.* **2013**, *12* (1), 237–252.

(122) Hasima, N.; Ozpolat, B. *Cell Death Dis.* **2014**, *5*, e1509.

(123) Adiwidjaja, J.; McLachlan, A. J.; Boddy, A. V. *Expert Opin. Drug Metab. Toxicol.* **2017**, *13* (9), 953–972.

(124) Zhao, G.; Dong, X.; Sun, Y. *Langmuir ACS J. Surf. Colloids* **2019**, *35* (5), 1846–1857.

(125) Yue, G.; Li, S.; Li, D.; Liu, J.; Wang, Y.; Zhao, Y.; Wang, N.; Cui, Z.; Zhao, Y. *Langmuir* **2019**, *35* (14), 4843–4848.

(126) Ahmadi Nasab, N.; Hassani Kumleh, H.; Beygzadeh, M.; Teimourian, S.; Kazemzad, M. *Artif. Cells Nanomedicine Biotechnol.* **2018**, *46* (1), 75–81.

(127) Agrawal, M.; Saraf, S.; Saraf, S.; Antimisiaris, S. G.; Chougule, M. B.; Shoyele, S. A.; Alexander, A. *J. Control. Release Off. J. Control. Release Soc.* **2018**, *281*, 139–177.

(128) Shahani, K.; Panyam, J. *J. Pharm. Sci.* **2011**, *100* (7), 2599–2609.

(129) Radhakrishnan, K.; Tripathy, J.; Datey, A.; Chakravortty, D.; Raichur, A. M. *New J. Chem.* **2015**, *39* (3), 1754–1760..

(130) Aras, A.; Khokhar, A. R.; Qureshi, M. Z.; Silva, M. F.; Sobczak-Kupiec, A.; Pineda, E. A. G.; Hechenleitner, A. A. W.; Farooqi, A. A. *Asian Pac. J. Cancer Prev. APJCP* **2014**, *15* (9), 3865–3871.

(131) Sunoqrot, S.; Al-Debsi, T.; Al-Shalabi, E.; Hasan Ibrahim, L.; Faruqu, F. N.; Walters, A.; Palgrave, R.; Al-Jamal, K. T. *ACS Biomater. Sci. Eng.* **2019**, *5* (11), 6036–6045.

(132) Monnier, A.; Schüth, F.; Huo, Q.; Kumar, D.; Margolese, D.; Maxwell, R. S.; Stucky, G. D.; Krishnamurty, M.; Petroff, P.; Firouzi, A.; Janicke, M.; Chmelka, B. *Science* **1993**, *261* (5126), 1299–1303.

(133) Jain, B. *J. Mol. Struct.* **2017**, *1130*, 194–198.

(134) Gangwar, R. K.; Tomar, G. B.; Dhumale, V. A.; Zinjarde, S.; Sharma, R. B.; Datar, S. *J. Agric. Food Chem.* **2013**, *61* (40), 9632–9637.

(135) Berlier, G.; Gastaldi, L.; Ugazio, E.; Miletto, I.; Iliade, P.; Sapino, S. *J. Colloid Interface Sci.* **2013**, *393*, 109–118.

(136) Jin, D.; Park, K.-W.; Lee, J. H.; Song, K.; Kim, J.-G.; Seo, M. L.; Jung, J. H. *J. Mater. Chem.* **2011**, *21* (11), 3641–3645.

(137) Du, X.; Zhang, M.; Meng, Q.; Song, Y.; He, X.; Yang, Y.; Han, J. *Opt. Express* **2010**, *18* (22), 22937–22943.

(138) Numata, Y.; Tanaka, H. *Food Chem.* **2011**, *126* (2), 751–755.

(139) Kolev, T. M.; Velcheva, E. A.; Stamboliyska, B. A.; Spiteller, M. *Int. J. Quantum Chem.* **2005**, *102* (6), 1069–1079.

(140) Mohan, P. R. K.; Sreelakshmi, G.; Muraleedharan, C. V.; Joseph, R. *Vib. Spectrosc.* **2012**, *62*, 77–84.

(141) Sanphui, P.; Goud, N. R.; Khandavilli, U. B. R.; Bhanoth, S.; Nangia, A. *Chem. Commun.* **2011**, *47* (17), 5013–5015.

(142) Van Nong, H.; Hung, L. X.; Thang, P. N.; Chinh, V. D.; Vu, L. V.; Dung, P. T.; Van Trung, T.; Nga, P. T. 2006, *SpringerPlus* 5 (1): 1147.

(143) Leung, M. H. M.; Pham, D.-T.; Lincoln, S. F.; Kee, T. W. *Phys. Chem. Chem. Phys.* **2012**, *14* (39), 13580.

(144) Singh, P. K.; Wani, K.; Kaul-Ghanekar, R.; Prabhune, A.; Ogale, S. *RSC Adv.* **2014**, *4* (104), 60334–60341.

(145) She, X.; Chen, L.; Yi, Z.; Li, C.; He, C.; Feng, C.; Wang, T.; Shigdar, S.; Duan, W.; Kong, L. *Mini Rev. Med. Chem.* **2018**, *18* (11), 976–989.

(146) Ebrahimifar, M.; Hasanzadegan Roudsari, M.; Kazemi, S. M.; Ebrahimi Shahmabadi, H.; Kanaani, L.; Alavi, S. A.; Izadi Vasfi, M. *Asian Pac. J. Cancer Prev.* **2017**, *18* (1), 65–68.

(147) Hashemzaei, M.; Delarami Far, A.; Yari, A.; Heravi, R. E.; Tabrizian, K.; Taghdisi, S. M.; Sadegh, S. E.; Tsarouhas, K.; Kouretas, D.; Tzanakakis, G.; Nikitovic, D.; Anisimov, N. Y.; Spandidos, D. A.; Tsatsakis, A. M.; Rezaee, R. *Oncol. Rep.* **2017**, *38* (2), 819–828.

(148) Santhosh, P. B.; Thomas, N.; Sudhakar, S.; Chadha, A.; Mani, E. *Phys. Chem. Chem. Phys. PCCP* **2017**, *19* (28), 18494–18504.

(149) Walters, D. K.; Muff, R.; Langsam, B.; Born, W.; Fuchs, B. *Invest. New Drugs* **2008**, *26* (4), 289–297.

(150) Catanzaro, D.; Ragazzi, E.; Vianello, C.; Caparrotta, L.; Montopoli, M. *Nat. Prod. Commun.* **2015**, *10* (8), 1365–1368.

(151) Elbialy, N. S.; Aboushoushah, S. F.; Sofi, B. F.; Noorwali, A. *Microporous Mesoporous Mater.* **2020**, *291*, 109540.

(152) Yang, P.; Gai, S.; Lin, J. *Chem. Soc. Rev.* **2012**, *41* (9), 3679–3698.

(153) Islami, F.; Sauer, A. G.; Miller, K. D.; Siegel, R. L.; Fedewa, S. A.; Jacobs, E. J.; McCullough, M. L.; Patel, A. V.; Ma, J.; Soerjomataram, I.; Flanders, W. D.; Brawley, O. W.; Gapstur, S. M.; Jemal, A. *CA. Cancer J. Clin.* **2018**, *68* (1), 31–54.

(154) Gao, Y.; Ding, S.; Huang, X.; Fan, Z.; Sun, J.; Hai, Y.; Li, K. *Drug Dev. Ind. Pharm.* **2019**, *45* (2), 273–281.